

# Wavelet Scattering Regression of Quantum Chemical Energies\*

Matthew Hirn<sup>†</sup>   Stéphane Mallat<sup>‡</sup>   Nicolas Poilvert<sup>§</sup>

May 4, 2022

## Abstract

We introduce multiscale invariant dictionaries to estimate quantum chemical energies of organic molecules, from training databases. Molecular energies are invariant to isometric atomic displacements, and are Lipschitz continuous to molecular deformations. Similarly to density functional theory (DFT), the molecule is represented by an electronic density function. A multiscale invariant dictionary is calculated with wavelet scattering invariants. It cascades a first wavelet transform which separates scales, with a second wavelet transform which computes interactions across scales. Sparse scattering regressions give state of the art results over two databases of organic planar molecules. On these databases, the regression error is of the order of the error produced by DFT codes, but at a fraction of the computational cost.

**Key words.** wavelet, scattering, multiscale, nonlinear regression, invariant dictionary, molecular energy, density functional theory, convolutional network

**AMS subject classifications.** 42C40, 42C15, 62J02, 62P35, 70F10, 81Q05, 41A05, 41A63

---

\*Submitted to the editors May 16, 2016. Revised version submitted October 24, 2016.

**Funding:** The research and manuscript preparation were supported by ERC grant InvariantClass 320959. During the revision of the manuscript, M.H. was partially supported by an Alfred P. Sloan Research Fellowship, a DARPA Young Faculty Award, NSF grant number 1620216, and additionally the Institute for Pure and Applied Mathematics (IPAM) during which time he was a resident.

<sup>†</sup>Michigan State University, Department of Computational Mathematics, Science & Engineering and Department of Mathematics, 428 South Shaw Lane, East Lansing, MI, 48824, USA, [mhirn@msu.edu](mailto:mhirn@msu.edu) (corresponding author)

<sup>‡</sup>École normale supérieure, Département d’Informatique, 45 rue d’Ulm, 75005 Paris, France

<sup>§</sup>The Pennsylvania State University, Millennium Science Complex, University Park, PA 16801, USA and BayLabs, Inc., [nicolas@baylabs.io](mailto:nicolas@baylabs.io)

# 1 Introduction

Computing the energy of a molecule given the charges and relative positions of its nuclei is a central topic in computational chemistry. It has important industrial applications such as molecular structure screening for improved organic photovoltaic materials [24] and predicting the thermodynamics and kinetics of industrially relevant chemical reactions [17]. Molecular energies are low lying eigenvalues of the molecular Hamiltonian operator, for the system of all interacting particles in the molecule. An exact numerical computation of molecular energies is beyond the capabilities of any computer for all but a handful of tiny molecules. Density functional theory [44] reduces the computation of ground state molecular energies by mapping the eigenvalue problem for the many-electron wavefunction to a variational problem over the total electronic density [27]. Nevertheless, the computational complexity remains considerable for large molecules. Much faster machine learning algorithms have been pioneered by several research groups, with surprisingly good results. Such algorithms for potential energy surface fitting of one molecule or material have been developed for more than two decades, tracing back to [45] with further contributions in [32, 8, 7, 42, 5, 49]. More recently machine learning algorithms have been developed to interpolate molecular energies across “chemical compound space,” fitting the potential energy surface across a range of molecules with different compositions [41, 46, 16]. In both cases molecular energies are regressed through interpolation over a database of known molecular energies. The precision of such algorithms depends upon the ability to reduce the dimensionality of the regression problem, by focusing on relevant variables. Efficient regression procedures take advantage of existing invariants [5]. We introduce a sparse multiscale wavelet scattering regression derived from known invariant and stability properties of molecular energies. State of the art numerical results are shown on databases of planar molecules.

Most computational chemistry approaches like density functional theory make use of the Born-Oppenheimer approximation, which models the atomic nuclei as classical particles, whereas electrons are considered as quantum particles. The state  $x = \{r_k, z_k\}_k$  of a molecule is thus defined by the position  $r_k \in \mathbb{R}^3$  of each nuclei and its charge  $z_k > 0$ . Section 2 briefly reviews the principles of density functional theory computations. A regression algorithm uses a training set of  $n$  molecular states  $\{x_i\}_{i \leq n}$  and their quantum energies  $\{f(x_i)\}_{i \leq n}$  to approximate the quantum energy  $f(x)$  of any molecule  $x$  within a given set  $\Omega$ . Such a regression  $\tilde{f}(x)$  can be calculated as a linear expansion over a dictionary  $\Phi(x) = (\phi_k(x))_k$  of functions of the molecular state  $x \in \Omega$ ,

$$\tilde{f}(x) = \langle w, \Phi(x) \rangle = \sum_k w_k \phi_k(x). \quad (1)$$

The regression vector  $w = (w_k)_k$  is computed by minimizing the training error  $\sum_{i \leq n} |f(x_i) - \tilde{f}(x_i)|^2$ , with some regularity condition imposed on its norm. Kernel and sparse regressions are reviewed in section 3.

The main difficulty is to find a dictionary  $\Phi(x)$  which produces a small average error  $|f(x) - \tilde{f}(x)|$  over all  $x \in \Omega$ . Since  $w$  is calculated from  $n$  training values,  $\tilde{f}$  belongs to an approximation space, not necessarily linear, of dimension smaller than the number  $n$  of training samples. The choice of  $\Phi(x) = (\phi_k(x))_k$  specifies the regularity of  $\tilde{f}(x)$ , which needs to match the regularity of  $f(x)$ .

A quantum energy functional  $f(x)$  satisfies elementary invariance and continuity properties relatively to geometric transformations of  $x$ , that we summarize:

1. **Permutation invariance:**  $f(x)$  is invariant to permutations of atom indices  $k$  in the state vector  $x = \{r_k, z_k\}_k$ .
2. **Isometric invariance:**  $f(x)$  is invariant to global translations, rotations, and symmetries of atomic positions  $r_k$ , and hence to any isometry [5].
3. **Deformation stability:**  $f(x)$  is Lipschitz continuous to variations of the distances  $|r_k - r_l|$  between atoms, and hence Lipschitz continuous to diffeomorphism actions [5].

We remark that the third property, deformation stability, excludes systems in which the potential energy surface abruptly changes. This phenomena occurs when electronic states cross, as can happen when a system goes from the ground state to an excited state after the absorption of a photon. However, most molecular systems left in their natural state will exhibit wide temperature and pressure ranges over which the deformation stability hypothesis is verified. We also emphasize that deformation stability, as described, does not include the nuclear charges  $\{z_k\}_k$ . These are considered discrete and we only consider the case of neutral molecular systems.

Dictionaries invariant to isometries are usually computed from the matrix of Euclidean atomic distances  $\{|r_k - r_l|\}_{k,l}$ . State of the art chemical energy regressions have been obtained with Coulomb kernels computed from these distances. However, section 3.1 shows that this representation is not invariant to permutations of the atom indices  $k$ , which introduces instabilities.

The goal of this paper is to introduce a dictionary  $\Phi(x)$  which is invariant to permutations and isometries, and Lipschitz continuous to diffeomorphism actions. It must also generate a space which is sufficiently large to provide accurate sparse energy regressions. Similarly to density functional theory, section 4 explains how to represent the molecular state  $x$  by an electronic density function  $\rho[x](u)$  of the spatial variable  $u \in \mathbb{R}^3$ . This density is invariant to atom index permutations and covariant to isometries. Invariance to isometries is then obtained by applying an invariant operator  $\Theta$ :

$$\Phi(x) = \Theta\rho[x].$$

The main difficulty is to define an operator  $\Theta$  which is also Lipschitz continuous to diffeomorphisms, and whose range is sufficiently large to regress large training databases. A tempting solution, used by several quantum energy regression algorithms [6, 5, 4, 46, 16], is to define  $\Theta$  from the autocorrelation or

the Fourier transform modulus of  $\rho$ . Section 5 explains why it yields instabilities to deformations, which degrades numerical regressions.

Building invariant dictionaries which are stable to diffeomorphism actions requires to separate variabilities at different scales. A large body of work has demonstrated the efficiency of multiscale modeling in quantum chemical systems [38, 47]. Multiscale wavelet transforms are used in some density functional theory softwares, to reduce computations by providing sparse representations of atomic wavefunctions [3, 37, 21, 44, 39, 48]. Section 6.1 defines wavelet norms which are invariant to isometries. Section 8 proves that Coulomb potential energies are regressed with much fewer wavelet invariants than Fourier invariants. Such wavelet expansions are similar to multipole decompositions [23, 22]. Quantum molecular energies also include exchange-correlation energy terms, responsible for the existence of chemical bonds, which are more complex than Coulomb potentials. The numerical results of section 7 show that wavelet invariants do not generate a sufficiently large approximation space to precisely regress these exchange-correlation energies.

Wavelet invariants perform a multiscale separation but do not take into account interactions across scales. Scattering invariants have been introduced in [31] to characterize these interactions with multiscale interference terms. They have found applications for image [43, 11] and audio [10, 2] signal classifications. Section 6.2 describes the resulting dictionary computed by transforming wavelet coefficient amplitudes, with a second wavelet transform. The resulting wavelet scattering dictionary remains invariant to isometries and Lipschitz continuous to diffeomorphism actions.

The accuracy of quantum energy regression with Coulomb kernels, Fourier, wavelet and scattering dictionaries is numerically evaluated in section 7, over databases of planar molecules. The planar symmetry reduces computations to two dimensions. It is shown that Coulomb kernel regression is approximately two times more accurate than Fourier and wavelet regressions. Second order scattering coefficients considerably reduce the error of wavelet regressions. It yields sparse expansions of quantum energy functionals. On these databases, the error is up to twice smaller than Coulomb kernel regressions and has an accuracy comparable to DFT numerical codes at a fraction of the computational cost.

## 2 Density Functional Theory

Density functional theory (DFT) provides relatively fast numerical schemes to compute the ground state energy of molecular systems. We summarize its methodology. Following the Born-Oppenheimer approximation, DFT models the nucleus of each atom as a classical particle, whereas electrons are considered as quantum particles. The total energy of a molecular state  $x = \{r_k, z_k\}_k$  is decomposed into:

$$\mathcal{E}(x) = E(x) + \frac{1}{2} \sum_{k \neq l}^K \frac{z_k z_l}{|r_k - r_l|}.$$

The second right hand side term is the Coulomb repulsion energy of all nuclei-nuclei interactions, considered as classical point-wise particles. The first term  $E(x)$  is the quantum energy resulting from electronic interactions. It is computed as an eigenvalue of the electronic Schrödinger equation:

$$H(x)\Psi = E(x)\Psi, \quad (2)$$

where  $H(x)$  is the Hamiltonian of the state  $x$  and  $\Psi(\bar{r}_1, \dots, \bar{r}_N)$  is a wavefunction which depends upon the positions of the  $N$  electrons of the molecule. The Hamiltonian is a sum of three terms:

$$H(x) = -\frac{1}{2} \sum_{j=1}^N \Delta_{\bar{r}_j} - \sum_{j=1}^N \sum_{k=1}^K \frac{z_k}{|\bar{r}_j - r_k|} + \frac{1}{2} \sum_{i \neq j}^N \frac{1}{|\bar{r}_i - \bar{r}_j|}.$$

These are respectively the electronic kinetic energy, the Coulomb electron-nuclei attraction energy, and the Coulomb electron-electron repulsion energy.

The Schrödinger equation (2) has many eigenvalues corresponding to quantized energies. The ground state energy corresponds to the lowest lying eigenvalue of a molecular state  $x$ , that we designate by  $E_0(x)$ :

$$f(x) = E_0(x) + \frac{1}{2} \sum_{k \neq l}^K \frac{z_k z_l}{|r_k - r_l|}. \quad (3)$$

Computing the Schrödinger eigenvalues requires a considerable amount of computations because  $\Psi(\bar{r}_1, \dots, \bar{r}_N)$  is a function of  $3N$  variables. Density functional theory considers instead the total electronic density as its unknown:

$$\rho(u) = \int_{\mathbb{R}^{3(N-1)}} |\Psi(u, \bar{r}_2, \dots, \bar{r}_N)|^2 d\bar{r}_2 \cdots d\bar{r}_N.$$

Since we consider the molecule to be electrically neutral, the sum of electronic charges is equal to the sum of the nuclei charges:

$$\int_{\mathbb{R}^3} \rho(u) du = N = \sum_k z_k.$$

Hohenberg and Kohn [27] proved that there exists a functional  $E_{\text{hk}}(\rho)$  of the electronic density, whose minimum is the ground state energy  $E_0(x)$ . In the Kohn-Sham approach to density functional theory [29], the total energy of the system is expressed as such a functional of the charge density:

$$E_{\text{hk}}(\rho) = \underbrace{T(\rho)}_{\text{Kinetic energy}} - \underbrace{\sum_{k=1}^K \int_{\mathbb{R}^3} \frac{z_k \rho(u)}{|u - r_k|} du}_{\text{External energy (electron-nuclei)}} + \underbrace{\frac{1}{2} \int_{\mathbb{R}^3} \int_{\mathbb{R}^3} \frac{\rho(u) \rho(v)}{|u - v|} du dv}_{\text{Hartree energy (electron-electron)}} + \underbrace{E_{\text{xc}}(\rho)}_{\text{Exchange correlation energy}}. \quad (4)$$

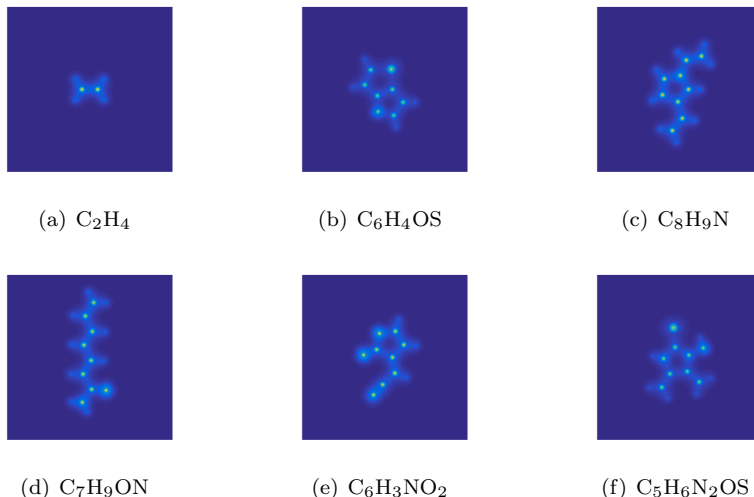


Figure 1: Ground state electronic density  $\rho_0[x]$  of planar molecules, in their plane.

The kinetic energy is not explicitly written as a functional of the density. Rather it is a functional of the Kohn-Sham orbitals, the square sum of which yields  $\rho$ . The exchange correlation energy regroups all of the quantum effects that result from collapsing the representation of the many body Schrödinger equation into a functional of the electronic density  $\rho$ . The ground state energy  $E_0(x)$  is obtained as the minimum value of  $E_{\text{hk}}(\rho)$  over all admissible electronic densities  $\rho$ . Its minimum value is reached at the ground state electronic density  $\rho_0[x]$  corresponding to the ground state electronic wavefunction  $\Psi_0$  of  $E_0(x)$ :

$$\rho_0[x] = \arg \min_{\text{admissible } \rho} E_{\text{hk}}(\rho) \quad \text{and} \quad E_0(x) = E_{\text{hk}}(\rho_0[x]).$$

Figure 1 shows examples of ground state electronic densities  $\rho_0[x]$  computed for several planar organic molecules. The observed "smearing" of the electronic density between nuclei is responsible for the presence of chemical bonds within the molecule.

The Kohn-Sham approach shows that the high-dimensional Schrödinger eigenvalue problem can be replaced by a variational problem over a three dimensional electronic density. In practical applications, the exchange correlation energy term is approximated, which leads to computational errors. However, density functional theory is most often used to compute molecular energies because it currently provides the best trade off between accuracy and computational complexity.

### 3 Energy Regression

Machine learning regressions are much faster procedures, which estimate the ground state energy  $f(x)$  of a molecular state  $x$ , by interpolating a database of ground state energies  $\{x_i, f(x_i)\}_i$ . This approach was pioneered by several groups [8, 41, 5, 46] who obtained impressive accuracy on different types of molecular databases. The next section describes Coulomb kernel ridge regressions, which give state of the art machine learning results on organic molecules. In this paper, we shall use sparse regressions, which are explained in section 3.2.

#### 3.1 Coulomb Kernel Regression

We introduce Coulomb kernel ridge regressions and discuss their invariance properties. A kernel ridge regression is a linear regression over the dictionary  $\Phi$ , given by  $\tilde{f}(x) = \langle w, \Phi(x) \rangle$ , where  $w = (w_k)_k$  is computed by minimizing the penalized error:

$$\sum_i |\tilde{f}(x_i) - f(x_i)|^2 + \lambda \sum_k |w_k|^2. \quad (5)$$

One can verify that the minimum is achieved for a  $w$  which can be written

$$w = \sum_i \alpha_i \Phi(x_i),$$

with

$$\tilde{f}(x) = \sum_{i=1}^n \alpha_i K(x, x_i) \quad \text{and} \quad K(x, x') = \langle \Phi(x), \Phi(x') \rangle.$$

The interpolation may thus directly be calculated from the kernel values  $K(x, x_i)$ , by finding the dual variables  $\{\alpha_i\}_i$  which minimize (5).

For quantum energy regressions,  $x = \{r_k, z_k\}_k$  gives the position and charge of each atom. The kernel must enforce the invariance to isometric transformations and the Lipschitz continuity to deformations. A Coulomb kernel [41] is calculated from the Coulomb energy potentials between all point charges  $(r_k, z_k)$  and  $(r_l, z_l)$  of  $x$ :

$$c_{k,l}(x) = \begin{cases} \frac{1}{2} z_k^{2.4}, & k = l, \\ \frac{z_k z_l}{|r_k - r_l|}, & k \neq l \end{cases}.$$

The resulting Coulomb kernel is

$$K(x, x') = \exp \left( -\frac{1}{\sigma} \sum_{k,l} |c_{k,l}(x) - c_{k,l}(x')| \right). \quad (6)$$

If the two molecules have a different number of atoms then the Coulomb matrix of the smallest molecule is extended with a zero padding.

Since the Coulomb kernel depends upon distances  $|r_k - r_l|$  it is invariant to isometries applied to atomic positions. A small deformation modifies these

distances by a multiplicative factor between  $1 - \epsilon$  and  $1 + \epsilon$ , where  $\epsilon$  measures the deformation size. Coulomb kernel values are thus modified by multiplicative factors which are of the same orders, and thus define a representation which is Lipschitz continuous to deformations.

However, Coulomb kernels are not invariant to permutations on the atom indices  $k$  [36]. This invariance can be enforced by ordering the columns and rows of the Coulomb matrix in decreasing order of their norm. However, this sorting may not be uniquely defined for symmetric molecules having several inter atomic distances of the same value, and it introduces instabilities. Small perturbations of atomic positions can indeed modify the ordering, thus breaking the deformation Lipschitz stability. This instability is reduced by calculating several Coulomb matrices, by adding a small random noise to the norms of rows and columns, which modifies their ordering. The regressed energy of a molecule is the average of regressed energies calculated over these different Coulomb matrices. This numerical technique reduces instabilities but does not eliminate them. However, these Coulomb kernel regressions nevertheless provide good approximations to ground state quantum molecular energies [41, 25].

### 3.2 Sparse Regression by Orthogonal Least Square

In this paper, we introduce sparse regressions in dictionaries  $\Phi(x) = (\phi_k(x))_k$  which are adapted to the properties of quantum energy functions  $f(x)$ . A linear regression is sparse in  $\Phi(x) = (\phi_k(x))_k$  if there are few, say  $M$ , non-zero regression coefficients  $w_k$ . The regression can then be written:

$$\tilde{f}(x) = \langle w, \Phi(x) \rangle = \sum_{m=1}^M w_{k_m} \phi_{k_m}(x).$$

The vector  $w$  is optimized in order to minimize the regression error  $\sum_{i \leq n} |f(x_i) - \tilde{f}(x_i)|^2$ , while imposing that the number of non-zero  $w_k$ , and hence the  $\ell^0$  norm of  $w$ , is smaller than  $M$ . Under appropriate hypothesis on  $\Phi(x)$ , this  $\ell^0$  norm penalization can be replaced by an  $\ell^1$  norm penalization, which is convex. However, these hypotheses are violated when  $\Phi(x) = (\phi_k(x))_k$  includes highly correlated functions [19, 18, 13]. This will be the case for quantum energy regression over wavelet or Fourier invariants. Sparse regression may however be computed with non-optimal greedy algorithms such as greedy orthogonal least square forward selections [14]. We describe this algorithm before concentrating on the construction of  $\Phi(x)$ .

A greedy least square algorithm selects the regression vectors one at a time, and decorrelates the dictionary relatively to the previously selected vectors. Let us denote by  $(\phi_k^m)_k$  the decorrelated dictionary at iteration  $m$ . We first select  $\phi_{k_m}^m$  from among  $(\phi_k^m)_k$ . We then decorrelate each  $\phi_k^m$  relatively to  $\phi_{k_m}^m$  over the training set  $\{x_i\}_i$ :

$$\tilde{\phi}_k^{m+1} = \phi_k^m - \left( \sum_i \phi_{k_m}^m(x_i) \phi_k^m(x_i) \right) \phi_{k_m}^m.$$

Each decorrelated vector is then normalized to define the updated dictionary:

$$\phi_k^{m+1} = \tilde{\phi}_k^{m+1} \left( \sum_i |\tilde{\phi}_k^{m+1}(x_i)|^2 \right)^{-1/2}.$$

The linear regression  $f_m(x)$  of  $f(x)$  is a projection on the first  $m$  selected vectors:

$$f_m(x) = \sum_{n=1}^m \tilde{w}_n \phi_{k_n}^n(x) \quad \text{with} \quad \tilde{w}_n = \sum_i f(x_i) \phi_{k_n}^n(x_i).$$

The  $m^{\text{th}}$  vector  $\phi_{k_m}^m$  is selected so that the training error  $\sum_i |f_m(x_i) - f(x_i)|^2$  is minimized. Since all projections are orthogonal,

$$\sum_i |f_m(x_i) - f(x_i)|^2 = \sum_i |f(x_i)|^2 - \sum_{n=1}^m |\tilde{w}_n|^2. \quad (7)$$

The error is thus minimized by choosing  $\phi_{k_m}^m$  which best correlates with  $f$ :

$$k_m = \arg \max_k \sum_i f(x_i) \phi_k^m(x_i).$$

The algorithm can be implemented with  $QR$  factorization, as described in [9], or directly as described above. In the latter case, the cost for each step is  $O(nK)$ , where  $n$  is the number of training samples  $x_i$  and  $K$  is the number of dictionary functions  $\phi_k$ . Since the algorithm selects  $M$  dictionary functions, the total cost is  $O(nKM)$ .

Since  $\phi_{k_m}^m$  is a linear combination of the  $\{\phi_{k_n}\}_{n \leq m}$ , the final  $M$ -term regression can also be written as a function of the  $\phi_{k_m}$  in the dictionary  $\Phi$ :

$$f_M(x) = \sum_{m=1}^M \tilde{w}_m \phi_{k_m}^m(x) = \sum_{m=1}^M w_m \phi_{k_m}(x). \quad (8)$$

Equation (8) is the orthogonal least square regression of  $f(x)$  over  $M$  vectors of  $\Phi(x)$ . This algorithm is used to represent quantum molecular energies over several dictionaries which are now defined.

## 4 Permutation Invariant Electronic Densities

To compute accurate sparse regressions of  $f(x)$  we must introduce a dictionary  $\Phi(x)$  which has the same invariance and regularity properties as  $f(x)$ . It must be invariant to isometries, and Lipschitz continuous to deformations, but also invariant to permutations of atom indices. Similarly to density functional theory, the molecular state  $x$  is represented by an electronic density  $\rho[x](u)$  for  $u \in \mathbb{R}^3$ . Invariance to isometries is then obtained by applying an invariant operator  $\Theta$ :

$$\Phi(x) = \Theta \rho[x].$$

This section concentrates on the calculation of  $\rho[x]$ , which must be invariant to permutations of atom indices and covariant to isometries. We cannot use the ground state molecular density  $\rho_0[x]$ , because its computation is as difficult as calculating the molecular ground state energy. We replace it by a much simpler non-interacting density, which adds the electron densities of isolated atoms. It does not include atomic interactions responsible for molecular bonds. The effect of these interactions on energy calculations will be incorporated through regression coefficients on  $\Phi(x)$ .

Each atom is in a neutral state, with  $z_k$  protons and  $z_k$  electrons. For example, Hydrogen and Oxygen atoms correspond respectively to  $z_k = 1$  and  $z_k = 8$ . The electronic density of such an isolated atom is a rotationally invariant function  $\rho[z_k](u)$ , with  $\int \rho[z_k](u) = z_k$ . The resulting non-interacting density of all atoms located at  $\{r_k\}_k$  is:

$$\rho[x](u) = \sum_{k=1}^K \rho[z_k](u - r_k). \quad (9)$$

Clearly  $\rho[x]$  is invariant to permutations of the indices  $k$ , and covariant to isometries. A deformation of atomic distances  $|r_k - r_l|$  produces a deformation of the atomic density  $\rho$ .

A model for the nuclei is obtained with a point charge  $\rho[z_k] = z_k \delta(u)$ , where each nucleus is treated as a classical particle. Section 8 shows that this model captures nuclei Coulomb interactions. As a model for the electrons,  $\rho[z_k] = z_k \delta(u)$  corresponds to aggregating all electrons at the position of the nucleus, which does not capture their quantum behavior. Defining  $\rho[z_k]$  as the exact electronic density of an isolated neutral atom with  $z_k$  protons is a more accurate model for the electronic density. It is computed numerically with a density functional theory software and stored.

A refinement, which better captures the chemical properties of each atom is to separate the density of core electrons  $\rho_{\text{cor}}$  from the density  $\rho_{\text{val}}$  of valence electrons. Indeed, chemical bonds are produced by valence electrons, whereas core electrons remain close to the nuclei and do not interact. In this case,  $\rho[z_k](u)$  is considered as a vector with two components  $(\rho_{\text{cor}}(u), \rho_{\text{val}}(u))$ . Section 7 shows that this separation provides a significant improvement of quantum energy regressions.

Figure 2(a) shows that the ground state electronic density  $\rho_0[x]$  is more delocalized along the bonds between atoms than the non-interacting electronic density in fig. 2(c), computed for individual atoms. The core electrons of the density in fig. 2(c) are shown in fig. 2(d). They are located close to the nuclei as in the Dirac model in fig. 2(b). Valence electrons in fig. 2(e) are more spread out.

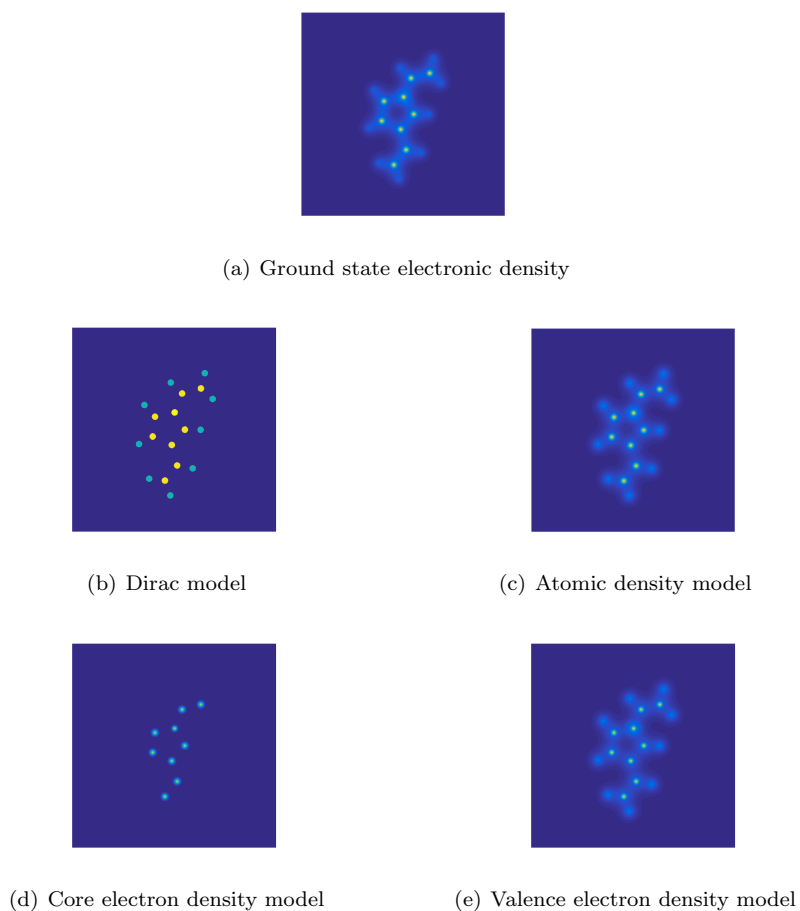


Figure 2: Electronic density and associated models.

(a): Ground state electronic density of the planar molecule  $C_8H_9N$ , restricted to its plane, and computed by DFT.

(b-e): Non-interacting density models, with a Dirac model in (b), an atomic density model computed by DFT in (c), which is subdivided into core electrons in (d) and into valence electrons in (e).

## 5 Invariant Fourier Modulus and Autocorrelations

Invariance to isometries is obtained by applying an operator  $\Theta$  to the electronic density model  $\rho$ . A Fourier transform modulus or an autocorrelation define translation invariant representations. Integrating over all rotations yields isometric invariant representations, which are used by several quantum energy regression algorithms [6, 5, 4, 46, 16]. We review the properties of these representations. They are invariant to permutations and isometries, but we show that they are unstable to deformations. This partly explains the limited performance of a Fourier modulus representation for quantum energy regressions, as shown by section 7.

The Fourier transform of a density  $\rho(u)$  is written for all  $\omega \in \mathbb{R}^3$ ,

$$\hat{\rho}(\omega) = \int_{\mathbb{R}^3} \rho(u) e^{-iu \cdot \omega} du.$$

Since the Fourier transform of  $\rho(u - \tau)$  is  $\hat{\rho}(\omega) e^{-i\tau \cdot \omega}$ , it results that  $|\hat{\rho}(\omega)|$  is translation invariant. It is also symmetry invariant. Indeed, if we define  $\bar{\rho}(u) = \rho(-u)$  then  $|\hat{\bar{\rho}}(\omega)| = |\hat{\rho}(\omega)|$ .

A rotation of  $\rho$  yields a rotation of its Fourier transform  $\hat{\rho}$ . A rotation invariant representation is obtained by averaging  $|\hat{\rho}(\omega)|$  over each rotation orbit, indexed by the sphere  $S^2$ . Let us represent  $\omega \in \mathbb{R}^3$  in spherical coordinates  $(\alpha, \eta)$  with  $\alpha = |\omega|$  and  $\eta \in S^2$ . We write  $\hat{\rho}(\omega) = \hat{\rho}_\alpha(\eta)$ . Rotation invariance is obtained by integrating  $|\hat{\rho}_\alpha(\eta)|^2$  over  $\eta \in S^2$ :

$$\|\hat{\rho}_\alpha\|_2^2 = \int_{S^2} |\hat{\rho}(\alpha\eta)|^2 d\eta.$$

For a non-interacting molecular density  $\rho[x](u) = \sum_k \rho[z_k](u - r_k)$ , Fourier invariants  $\|\hat{\rho}_\alpha\|_2^2$  depend upon atomic positions  $r_k$  through inter-atomic distances  $|r_k - r_l|$ . Indeed,

$$|\hat{\rho}(\omega)|^2 = \sum_{k,l} \hat{\rho}[z_k](\omega) \hat{\rho}[z_l]^*(\omega) e^{-i(r_k - r_l) \cdot \omega}.$$

Since  $\rho[z_k](u)$  is rotationally invariant,  $\hat{\rho}[z_k](\omega)$  is also rotationally invariant. Integrating  $|\hat{\rho}(\alpha\eta)|^2$  over  $\eta \in S^2$  thus only depends on  $r_k$  through all  $|r_k - r_l|$ . These Fourier invariants thus define a distance embedding which is invariant to index permutations, as opposed to Coulomb matrices, but they are not stable to deformations.

Section 8 proves, essentially, that the Coulomb energy of nuclei and electronic densities can be regressed linearly, with an error  $O(\epsilon)$ , over a dictionary of Fourier invariants of size  $O(\epsilon^{-2})$ . The radial frequency parameter  $\alpha$  is sampled at intervals  $\epsilon$  over a frequency range  $\alpha \in [\epsilon, \epsilon^{-1}]$ . It yields  $\epsilon^{-2}$  Fourier invariants  $\{\|\hat{\rho}_{k\epsilon}\|_2^2\}_{1 \leq k \leq \epsilon^{-2}}$ . However, quantum energy functionals also include

more complex exchange correlation terms. The resulting energy stored in so-called chemical bonds grows rather linearly than quadratically with the number of electrons. To approximate these terms, we include  $\mathbf{L}^1$  norms, which are also invariant to isometries:

$$\|\hat{\rho}_\alpha\|_1 = \int_{S^2} |\hat{\rho}(\alpha\eta)| d\eta.$$

The resulting Fourier modulus dictionary is defined by:

$$\Theta\rho = \left( \|\hat{\rho}_{k\epsilon}\|_1, \|\hat{\rho}_{k\epsilon}\|_2^2 \right)_{0 \leq k \leq \epsilon^{-2}}. \quad (10)$$

If  $\rho$  is defined by core and valence electron densities, then these norms are computed separately over core and valence densities, which multiplies by two the number of invariants.

A major drawback of Fourier invariants is their instability to deformations. Let  $D_\tau\rho(u) = \rho(u - \tau(u))$  be a deformation of a density  $\rho(u)$ . The amplitude of such a deformation is given by the matrix norm of the Jacobian  $\nabla\tau$ , which is written  $\|\nabla\tau\|_\infty$ . If  $\|\nabla\tau\|_\infty < 1$  then  $u - \tau(u)$  is a diffeomorphism. Lipschitz continuity to deformation means that there exists  $C > 0$  such that for all  $\rho \in \mathbf{L}^2(\mathbb{R}^3)$ ,

$$\|\Theta\rho - \Theta D_\tau\rho\|_2 \leq C \|\nabla\tau\|_\infty \|\rho\|_2, \quad (11)$$

with  $\|\rho\|_2^2 = \int |\rho(u)|^2 du$ . The distance thus decreases to zero when the deformation amplitude  $\|\nabla\tau\|_\infty$  goes to zero. The factor  $\|\rho\|_2$  is an amplitude normalization.

It is well known that the Fourier transform modulus does not satisfies this Lipschitz continuity property. Consider a dilation  $\tau(u) = \epsilon u$ , for which  $\|\nabla\tau\|_\infty = \epsilon$ . In this case  $\widehat{D_\tau\rho}(\omega) = (1 + \epsilon)^{-1} \hat{\rho}(\omega(1 + \epsilon)^{-1})$  so a frequency  $\omega_0$  is “moved” by about  $\epsilon\omega_0$ , which is large if  $\omega_0 \gg \epsilon^{-1}$ . For any  $C > 0$ , one can then easily construct  $\hat{\rho}$  concentrated around a frequency  $\omega_0$  so that  $\|\widehat{|\hat{\rho}|} - |\widehat{D_\tau\rho}|\|_2$  does not satisfy (11), because the right hand-side decreases linearly with  $\epsilon$  [31]. The rotation invariance integration does not eliminate this instability so  $\Theta$  is not Lipschitz continuous to deformations.

One may replace the Fourier modulus dictionary by an autocorrelation as in SOAP energy regressions [6, 5, 4, 16]:

$$A\rho(\tau) = \rho * \bar{\rho}(\tau) \quad \text{with} \quad \bar{\rho}(u) = \rho(-u),$$

but it has essentially the same properties. It is also translation invariant and its Fourier transform is  $|\hat{\rho}(\omega)|^2$ . For an electronic density, we get

$$A\rho[x](\tau) = \sum_{k,l} \rho[z_k] * \bar{\rho}[z_l](\tau - (r_k - r_l)).$$

Rotation invariance is obtained by representing  $\tau$  in spherical coordinates  $(\alpha, \eta)$ , with  $\alpha = |\tau|$ ,  $\eta \in S^2$ , and integrating over  $\eta$ :

$$\bar{A}\rho[x](\alpha) = \int_{S^2} A\rho[x](\alpha\eta) d\eta = \sum_{k,l} \int_{S^2} \rho[z_k] * \bar{\rho}[z_l](\alpha\eta - (r_k - r_l)) d\eta.$$

Since each  $\rho[z_k]$  is a rotationally symmetric bump, it is a sum of bumps centered at  $|r_k - r_l|$ . It is thus invariant to isometries acting on  $x$ . The width of each bump is below a constant  $\sigma$  which measures the maximum spread of valence electrons of individual atoms.

Instabilities to deformations  $D_\tau \rho(u) = \rho(u - \tau(u))$  can be seen with a dilation  $\tau(u) = (1 + \epsilon)u$ . This dilation moves each bump located at  $|r_k - r_l|$  by  $\epsilon|r_k - r_l|$ . For long distances  $|r_k - r_l| \gg \sigma/\epsilon$ , the bumps produced by the deformed density have non-overlapping support with the original bumps. It results that  $\|\bar{A}\rho - \bar{A}D_\tau \rho\|_2$  does not decrease proportionally to  $\|\nabla u\|_\infty = \epsilon$ , uniformly over all densities  $\rho$ . Similarly to the Fourier modulus, autocorrelation invariants are not Lipschitz continuous to deformations.

Deformation instabilities can be controlled by imposing that the maximum distance  $|r_k - r_l|$  is bounded by a constant which is not too large. This strategy is adopted by local autocorrelations used by Smooth Overlap of Atomic Positions (SOAP) representations [5]. However, this limits the interaction distances between atoms, which means that one can only regress energies resulting from short range interactions, while being stable to deformations.

## 6 Invariant Wavelet Scattering

Wavelet transforms avoid the deformation instabilities of Fourier transforms, by separating different scales. We first introduce wavelet transform invariants while explaining their limitations to regress complex functionals. Wavelet scattering transforms address these issues by introducing multiscale interaction terms.

### 6.1 Invariant Wavelet Modulus

A wavelet transform separates the variations of a function along different scales and orientations. It is computed by dilating and rotating a mother wavelet  $\psi : \mathbb{R}^3 \rightarrow \mathbb{C}$  having a zero average. We denote by  $r_\theta \in \text{O}(3)$  an orthogonal operator in  $\mathbb{R}^3$ , indexed by a three-dimensional angular parameter  $\theta$ . Applying it to  $\psi$  at different scales  $2^j$  gives:

$$\psi_{j,\theta}(u) = 2^{-3j} \psi(2^{-j} r_\theta^{-1} u).$$

The wavelet transform of  $\rho \in \mathbf{L}^2(\mathbb{R}^3)$  computes  $\rho * \psi_{j,\theta}$ . The Fourier transform of  $\psi_{j,\theta}$  is:

$$\widehat{\psi}_{j,\theta}(\omega) = \widehat{\psi}(2^j r_\theta^{-1} \omega).$$

If  $\widehat{\psi}(\omega)$  has its support centered in the neighborhood of a frequency  $\omega_0$  then  $\widehat{\psi}_{j,\theta}$  has a support located in the neighborhood of  $2^{-j} r_\theta \omega_0$ .

Similarly to the Fourier transform, we compute invariants from the modulus of wavelet coefficients  $|\rho * \psi_{j,\theta}(u)|$ . If  $\psi^*(u) = \psi(-u)$ , where  $\psi^*(u)$  denotes the complex conjugate of  $\psi(u)$ , then  $|\rho * \psi_{j,-\theta}| = |\rho * \psi_{j,\theta}|$ . Suppose that  $\psi(u)$  is invariant to two-dimensional rotations around a symmetry axis defined by  $\eta_0 \in S^2$ , and thus satisfies  $\psi(r_\theta u) = \psi(u)$  if  $r_\theta \eta_0 = \eta_0$ . All numerical

computations are performed with Morlet wavelets, which are examples of such symmetrical wavelets:

$$\psi(u) = e^{-|u|^2/2}(e^{i\eta_0 \cdot u} - C),$$

where  $C$  is chosen so that  $\int \psi(u) du = 0$ . The wavelet  $\psi_{j,\theta}$  only depends upon the value of  $\eta = r_\theta \eta_0 \in S^2$ , modulo a sign. All rotations  $r_\theta$  which modify a wavelet can thus be indexed by a two-dimensional Euler angular parametrisation  $\theta \in [0, \pi]^2$  of the half sphere.

Wavelet coefficients are computed up to a maximum scale  $2^J$ . Frequencies below  $2^{-J}|\eta_0|$  are captured by a low-pass filter  $\phi_J(u) = 2^{-3J}\phi(2^{-J}u)$  where  $\phi(u) \geq 0$  is a positive rotationally symmetric function, with  $\int \phi(u) du = 1$ . Its Fourier transform  $\hat{\phi}(\omega)$  is essentially concentrated in the ball  $|\omega| \leq |\eta_0|$ . Often  $\phi(u)$  is chosen to be a Gaussian. The resulting wavelet transform operator is defined by:

$$W\rho = \left\{ \rho * \phi_J, \rho * \psi_{j,\theta} \right\}_{j < J, \theta \in [0, \pi]^2}.$$

The Fourier transform of  $\psi$  is assumed to satisfy the following Littlewood-Paley condition for some  $0 \leq c < 1$  and all  $\omega \neq 0$ :

$$1 - c \leq |\hat{\phi}(2^J \omega)|^2 + \sum_{j < J} \int_{[0, \pi]^2} |\hat{\psi}(2^j r_\theta^{-1} \omega)|^2 d\theta \leq 1.$$

Applying the Plancherel formula proves that

$$(1 - c) \|\rho\|_2^2 \leq \|\rho * \phi_J\|_2^2 + \sum_{j < J} \int_{[0, \pi]^2} \int_{\mathbb{R}^3} |\rho * \psi_{j,\theta}(u)|^2 du d\theta \leq \|\rho\|_2^2.$$

It results that  $W$  is a stable and invertible operator on  $\mathbf{L}^2(\mathbb{R}^3)$ .

For an electronic density  $\rho[x](u) = \sum_k \rho[z_k](u - r_k)$ ,

$$|\rho[x] * \psi_{j,\theta}(u)| = \left| \sum_k \rho[z_k] * \psi_{j,\theta}(u - r_k) \right|.$$

A wavelet modulus coefficient thus gives the amplitude at  $u$  of interferences produced by wavelets of scale  $2^j$  “emitted” by each charge density  $\rho[z_k]$  centered at  $r_k$ ; see fig. 3.

The wavelet transform modulus is invariant to symmetries. If  $\bar{\rho}(u) = \rho(-u)$  then  $|\rho * \psi_{j,\theta}(u)| = |\bar{\rho} * \psi_{j,\theta}(u)|$  because  $\psi(-u) = \psi^*(u)$ . It is covariant to translations and rotations but not invariant. Translation and rotation invariant dictionaries are obtained by integrating  $|\rho * \psi_{j,\theta}(u)|^2$  over the translation and rotation variables:

$$\|\rho * \psi_{j,\cdot}\|_2^2 = \int_{\mathbb{R}^3 \times [0, \pi]^2} |\rho * \psi_{j,\theta}(u)|^2 du d\theta.$$

The Plancherel formula gives

$$\|\rho * \psi_{j,\cdot}\|_2^2 = \frac{1}{(2\pi)^3} \int_{\mathbb{R}^3 \times [0, \pi]^2} |\hat{\rho}(\omega)|^2 |\hat{\psi}(2^j r_\theta^{-1} \omega)|^2 d\omega d\theta.$$

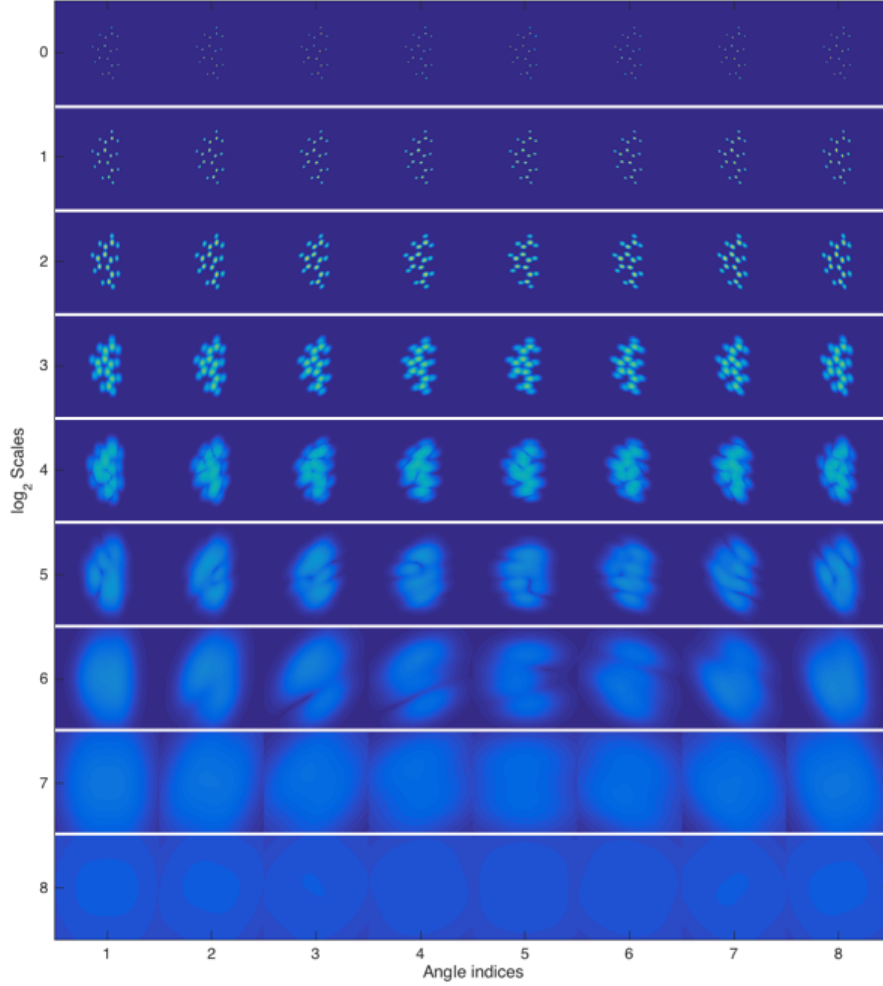


Figure 3: Wavelet modulus transform  $|\rho * \psi_{j,\theta}|$  of the molecule in fig. 2, visualized over  $\log_2$  scales  $j = 0, \dots, 8$  and eight two dimensional rotations sampled uniformly from the half circle  $[0, \pi)$ . Rotations are indexed on the horizontal axis, while scales get progressively larger as one moves down the vertical axis. Wavelet invariants such as  $\|\rho * \psi_{j,\cdot}\|_1$  aggregate all of the spatial and rotational information from each row into a single wavelet coefficient.

It computes the energy of  $|\hat{\rho}(\omega)|^2$  around the sphere of radius  $2^{-j}|\eta_0|$ , over an annulus of width of the order of  $2^{-j}|\eta_0|$ . This frequency integral is much more delocalized than the Fourier integral  $\|\hat{\rho}_\alpha\|^2$  which gives the energy of  $|\hat{\rho}(\omega)|^2$  exactly on the sphere of radius  $\alpha$ . The index  $-j$  can be interpreted as a log radial frequency variable. These wavelet quadratic invariants have a much lower frequency resolution than Fourier invariants at high frequencies.

Similarly to the Fourier dictionary (10), the range of radial frequencies is defined over an interval  $[\epsilon, \epsilon^{-2}]$  for some  $\epsilon > 0$ . Over this interval, there are only  $3|\log_2 \epsilon|$  scales defined by  $2\log_2 \epsilon \leq j < -\log_2 \epsilon = J$ . For appropriate wavelets, section 8 proves Coulomb energies can be regressed with an  $O(\epsilon)$  error from these  $3|\log_2 \epsilon|$  wavelet invariants. Such a regression is much more sparse than a Fourier regression which requires  $O(\epsilon^{-2})$  terms to obtain an  $O(\epsilon)$  error.

To regress molecular energy functionals, which include exchange correlation energy terms, like the Fourier dictionary (10) we include  $\mathbf{L}^1$  invariants:

$$\|\rho * \psi_{j,\cdot}\|_1 = \int_{\mathbb{R}^3 \times [0, \pi]^2} |\rho * \psi_{j,\theta}(u)| du d\theta,$$

at scales  $2^j < 2^J$ . At the lowest frequencies we get  $\|\rho * \phi_J\|_1$ . Since  $\rho \geq 0$  and  $\phi_J \geq 0$  with  $\int \phi_J(u) du = 1$ , it results that  $\|\rho * \phi_J\|_1 = \|\rho\|_1$  is the total electronic charge. The resulting invariant wavelet dictionary, up to a highest frequency  $\epsilon^{-2}$  is:

$$\Theta\rho = \left\{ \|\rho\|_1, \|\rho * \psi_{j,\cdot}\|_1, \|\rho * \psi_{j,\cdot}\|_2^2 \right\}_{2\log_2 \epsilon \leq j < J}. \quad (12)$$

As opposed to Fourier, wavelets yields invariants which are stable to deformations. It is proved in [31] that such wavelet invariants are Lipschitz continuous to the action of  $\mathbf{C}^2$  diffeomorphisms. Indeed, wavelets are localized in space. Computing the wavelet transform of a deformed  $\rho$  is equivalent to computing the wavelet transform of  $\rho$  with deformed wavelets. Since wavelets have a localized support, a deformation is locally equivalent to a small dilation and rotation, which produces a small modification of  $\mathbf{L}^2$  or  $\mathbf{L}^1$  norms.

Section 7 shows that quantum energy regressions over this wavelet invariant dictionary produces a similar error as regression over Fourier invariants (10), but with far fewer terms. The error is not much reduced because this dictionary does not include enough invariants to regress the complex behavior of exchange correlation energy terms.

## 6.2 Multiscale Scattering Invariants

A wavelet transform is invertible but integrating its modulus along spatial and rotation variables does not produce enough invariants. Wavelet scattering operators have been introduced in [31] to define much richer sets of invariants, with higher order multiscale interference terms.

Integrating wavelet modulus coefficients

$$\|\rho * \psi_{j,\cdot}\|_1 = \int_{\mathbb{R}^3 \times [0, \pi]^2} |\rho * \psi_{j,\theta}(u)| du d\theta,$$

removes the variability of  $|\rho * \psi_{j,\theta}(u)|$  along  $u \in \mathbb{R}^3$  and  $\theta \in [0, \pi]^2$ . This variability can be captured by computing the wavelet transform of  $|\rho * \psi_{j,\theta}(u)|$  along both  $u$  and  $\theta$ , which defines a scattering transform on the roto-translation group [43]. In the following, we concentrate on the variability along  $u$  and thus only compute scattering coefficients along the translation variable  $u \in \mathbb{R}^3$  [31].

The variations of  $|\rho * \psi_{j,\theta}(u)|$  along  $u$  are represented by a second wavelet transform, which computes convolutions with a second family of wavelets at different scales  $2^{j'}$  with rotations of angles  $\theta + \theta' \in [0, \pi]^2$ :

$$||\rho * \psi_{j,\theta} * \psi_{j',\theta'+\theta}(u)|.$$

Such a coefficient computes the first order interferences  $|\rho * \psi_{j,\theta}(u)|$  of the variations of  $\rho$  at a scale  $2^j$  along the orientation  $\theta$ . These interference amplitudes interfere again by “emitting” a new wavelet of scale  $2^{j'}$  whose angle is incremented by  $\theta'$ . It yields second order interferences, whose amplitudes are measured at each position  $u$ . The Fourier transform of  $|\rho * \psi_{j,\theta}(u)|$  has an energy mostly concentrated at frequencies  $|\omega| < 2^{-j}|\eta_0|$ . As a result, the amplitude of these second order coefficients is non-negligible only if  $2^{j'} > 2^j$ .

Invariance to translations and rotations is obtained by integrating along  $(u, \theta) \in \mathbb{R}^3 \times [0, \pi]^2$ :

$$|||\rho * \psi_{j,\cdot} * \psi_{j',\theta'+\cdot}|_1 = \int_{\mathbb{R}^3 \times [0, \pi]^2} ||\rho * \psi_{j,\theta}(u) * \psi_{j',\theta'+\theta}(u)| du d\theta.$$

A coefficient  $|||\rho * \psi_{j,\cdot} * \psi_{j',\theta'+\cdot}|_1$  computes the interaction amplitudes of variations of  $\rho$  at a scale  $2^j$  along the orientation  $\theta$ , located at a distance about  $2^{j'}$  within an orientation  $\theta' + \theta$ . It provides a rich set of invariants, which depend upon the multiscale geometry of the charge density  $\rho$ .

Quadratic terms are obtained by integrating the squared amplitude of second order coefficients:

$$|||\rho * \psi_{j,\cdot} * \psi_{j',\theta'+\cdot}|_2^2 = \int_{\mathbb{R}^3 \times [0, \pi]^2} ||\rho * \psi_{j,\theta}(u) * \psi_{j',\theta'+\theta}(u)|^2 du d\theta.$$

A scattering transform further iterates this procedure by computing higher order terms obtained through convolutions with third order wavelets and more. Because it cascades wavelet transforms, it is proved in [31] that a scattering transform remains Lipschitz continuous to diffeomorphism actions. In this paper, we only keep second order terms for regressions.

Wavelet scales are computed over a frequency range defined by  $2^J > 2^{j'} > 2^j \geq \epsilon^2$ . Adding second order terms to the invariant wavelet dictionary (12) defines a second order wavelet scattering dictionary:

$$\begin{aligned} \Theta\rho = & \left\{ ||\rho||_1, ||\rho * \psi_{j,\cdot}||_1, ||\rho * \psi_{j,\cdot}||_2^2, \right. \\ & \left. |||\rho * \psi_{j,\cdot} * \psi_{j',\theta'+\cdot}|_1, |||\rho * \psi_{j,\cdot} * \psi_{j',\theta'+\cdot}|_2^2 \right\}_{2^{\log_2 \epsilon \leq j < j' < J, \theta' \in [0, \pi]^2}}. \end{aligned} \quad (13)$$

This dictionary is invariant to permutations of atom indices, to isometries and is Lipschitz continuous to deformations. The next section shows that it considerably outperforms Fourier modulus and wavelet representations for quantum energy regressions.

Second layer scattering coefficients are a priori indexed by a four dimensional parameter  $(j, j', \theta') \in \mathbb{Z} \times \mathbb{Z} \times [0, \pi]^2$ . Appendix A proves that the two dimensional angle parameter  $\theta'$  can be reduced to a one dimensional angle parameter. Consider the second order term  $|\rho * \psi_{j,\theta}| * \psi_{j',\theta'+\theta}|$ . If  $\eta \in S^2$  is the axis corresponding to  $\theta$  and  $\eta' \in S^2$  is the axis corresponding to  $\theta' + \theta$ , then after integrating over  $\theta$  the only distinguishing parameter is the angle between  $\eta$  and  $\eta'$  (which is constant for all  $\theta$ ). Indeed, since scattering coefficients (13) are invariant to rigid motions, a single rotation applied to both  $\eta$  and  $\eta'$  will not change their value.

Appendix A also precisely describes the symmetries of the wavelet  $\psi$  and the corresponding wavelet modulus transform  $|\rho * \psi_{j,\theta}|$  and second order scattering transform  $|\rho * \psi_{j,\theta}| * \psi_{j',\theta'+\theta}|$ . The approach in the appendix is used to not only prove the aforementioned result, but also gives insight into how one can efficiently compute scattering coefficients by fully taking into account the built in symmetries.

## 7 Numerical Energy Regression of Planar Molecules

We compare the performance of Coulomb kernel regressions with Fourier, wavelet and scattering regressions, on two databases of planar organic molecules which are in their equilibrium configuration. The planar symmetry allows us to reduce computations in two dimensions, as explained in the next section.

We remark that in most applications the equilibrium structure of the molecule is not known, but rather must be found by computing the partial derivatives of the total energy with respect to the atomic positions  $\{r_k\}_k$ , i.e. the ionic forces. If the dictionary functions  $\{\phi_k\}_k$  are smooth and the gradient  $\nabla\phi_k$  can be computed for each  $k$ , then the ionic forces can be incorporated into the regression via:

$$\nabla\tilde{f}(x) = \sum_k w_k \nabla\phi_k(x).$$

The gradients  $\{\nabla\phi_k\}_k$  can be computed analytically for the scattering dictionary. We omit the details here, since they are not used in these numerical experiments. However, such computations can be used, for example, to extend scattering regressions for the purpose of calculating equilibrium configurations corresponding to local minima in the potential energy surface.

All numerical results can be reproduced by visiting:

<https://github.com/matthew-hirn/ScatNet-QM-2D>

and downloading the **ScatNet-QM-2D** package, which includes all software and data.

## 7.1 Representation of Planar Molecules

For planar molecules  $x$ , the positions  $\{r_k\}_k$  of the atom nuclei are in a two-dimensional plane. Since the energy is invariant to rotations, it only depends upon the relative nuclei positions in this plane. The molecule geometry can thus be represented in two as opposed to three dimensions. Suppose that the  $r_k$  correspond to the two-dimensional positions of the nuclei in the plane  $\mathbb{R}^2$ . The electronic density  $\rho[x] = \sum_k \rho[z_k](u - r_k)$  can then be restricted to  $\mathbb{R}^2$ . The invariant dictionary  $\Phi(x) = \Theta\rho[x]$  is computed by applying an operator  $\Theta$  on  $\rho[x](u)$ , for  $u \in \mathbb{R}^2$  as opposed to  $\mathbb{R}^3$ . Fourier, wavelet and scattering dictionaries are therefore computed in two dimensions. Although it does not change the nature of the regression problem, it reduces computations in numerical experiments.

There are several ways to restrict the isolated electronic densities  $\rho[z_k]$  to  $\mathbb{R}^2$ . We derive the two dimensional density from the three dimensional one by condensing the charge mass on the sphere of radius  $\alpha$  to the circle of radius  $\alpha$ . Note that since the isolated charge densities are radially symmetric, the value  $\rho[z_k](u)$  depends only on  $|u|$ , i.e.,  $\rho[z_k](u) = \rho[z_k](\alpha)$  for  $\alpha = |u|$ . The total charge  $z_k$  can therefore be decomposed over spheres of radius  $\alpha$  as follows:

$$z_k = \int_{\mathbb{R}^3} \rho[z_k](u) du = \int_0^\infty 4\pi\alpha^2 \rho[z_k](\alpha) d\alpha. \quad (14)$$

A radially symmetric two-dimensional electronic density,  $\rho_{2D}[z_k] : \mathbb{R}^2 \rightarrow \mathbb{R}$ , with total charge  $z_k$ , can be decomposed similarly:

$$z_k = \int_{\mathbb{R}^2} \rho_{2D}[z_k](u) du = \int_0^\infty 2\pi\alpha \rho_{2D}[z_k](\alpha) d\alpha. \quad (15)$$

Equating the two integrands of (14) and (15) yields:

$$\forall \alpha \in [0, \infty), \quad \rho_{2D}[z_k](\alpha) = 2\alpha\rho[z_k](\alpha).$$

In two dimensions, reflections are not generated via  $-I$  (where  $I$  is the identity matrix) as in  $\mathbb{R}^3$ , but rather through a fixed reflection about a line, for example the horizontal or vertical axis. Therefore, if  $\tilde{\rho}$  is a reflection of  $\rho$ ,

$$\|\tilde{\rho} * \psi_{j,\cdot} | * \psi_{j',\theta'+\cdot}\|_p^p = \|\rho * \psi_{j,\cdot} | * \psi_{j',-\theta'+\cdot}\|_p^p,$$

where the angles  $\theta, \theta'$  now parameterize the half circle  $S^1$ , taken as  $(-\pi/2, \pi/2]$ . Two dimensional reflections thus reflect the second order angle parameter  $\theta'$ , mapping it to  $-\theta'$ . Invariant second order scattering coefficients are obtained by taking the average:

$$\forall \theta' \in [0, \pi/2], \quad p = 1, 2, \quad \frac{1}{2} \sum_{\varepsilon=-1,1} \|\rho * \psi_{j,\cdot} | * \psi_{j',\varepsilon\theta'+\cdot}\|_p^p.$$

In numerical computations, electronic densities  $\rho[x]$  are sampled at sufficiently small intervals  $\epsilon$ . In the following, we normalize this sampling interval

to 1. Electronic densities  $\rho[x]$  are sampled over a square of  $2^{2J}$  samples, with  $2^J = 2^9$ . The Fourier dictionary (10) is computed with a two-dimensional Fourier transform. The modulus and squared Fourier transform modulus are integrated over the unit frequency circle  $S^1$ , to achieve rotation invariance. The resulting dictionary has  $2^{J-1} = 2^8$  radial Fourier invariants per density channel (as described in section 4).

The wavelet dictionary (12) is computed with a wavelet transform over  $J = 9$  scales  $2^j$ ,  $j = 0, \dots, 8$ , with  $\mathbf{L}^1$  and  $\mathbf{L}^2$  norms. The angular variable is also integrated over the circle  $S^1$ . The wavelet dictionary thus has  $2J + 1 = 19$  wavelet invariants per density channel.

The scattering dictionary (13) also includes second order invariants, which are indexed by two scale indices  $0 \leq j < j' < J$ . In two dimensions, the angle  $\theta$  is discretized over  $L$  values in  $(-\pi/2, \pi/2]$ . In numerical computations,  $L = 16$ . Second order terms include  $\mathbf{L}^1$  and  $\mathbf{L}^2$  invariants. The total number of second order scattering functions is thus  $(L/2 + 1)J(J - 1)$ . The wavelet scattering dictionary therefore has  $1 + 2J + (L/2 + 1)J(J - 1) = 667$  invariants per density channel.

For the parameters listed previously and using an iMac desktop with a 4 GHz Intel Core i7 processor and 32 GB 1600 MHz DDR3 random access memory (RAM), the walltime cost of computing the  $\mathbf{L}^1$  and  $\mathbf{L}^2$  scattering coefficients for a single molecule is approximately 45 seconds. The wavelet filters  $\psi_{j,\theta}$  are implemented as a filter bank, which requires a one time computation whose walltime is approximately 25 seconds. The wavelet coefficients  $\rho * \psi_{j,\theta}(u)$  are computed in frequency, leveraging the fact that  $\widehat{\rho * \psi_{j,\theta}}(\omega) = \widehat{\rho}(\omega)\widehat{\psi_{j,\theta}}(\omega)$ . Using the fast Fourier transform (FFT) and inverse FFT, the cost per molecule is  $O(LJ^22^{2J})$  to compute the wavelet invariants. Scattering invariants are computed in a similar fashion, but with a computational cost of  $O(L^2J^32^{2J})$  that reflects the additional second order invariants. Increasing the angle parameter  $L$  increases the accuracy of the approximate integral over the rotation group and also increases the number of second order scattering invariants; however, it does not in general depend on the type of molecule. The scale parameter  $J$  grows with the size of the largest molecule. Typically in two dimensions the relationship is  $J \sim \frac{1}{2} \log_2 K$ , where  $K$  is the number of atoms, although specific types of molecules may scale differently (for example, a string of atoms arranged linearly will scale as  $J \sim \log_2 K$ , although in this case one could replace the square grid with a rectangular one).

## 7.2 Numerical Comparison Over Planar Molecules

We compare the regression performance of Fourier, wavelet and scattering dictionaries over two databases of planar molecules. The molecular atomization energies in these databases were computed using the hybrid density functional PBE0 [1]. The errors of such hybrid DFT methods are in the range of 3 to 5 kcal/mol [40, 28] relative to experimental energies (mean absolute error). The first database includes 454 nearly planar molecules among the 7165 molecules

Table 1: Average Error  $\pm$  Standard Deviation over the five folds in kcal/mol, with a Coulomb kernel regression and sparse regressions in Fourier, wavelet and scattering dictionaries. For scattering dictionaries, regressions are computed for several densities  $\rho[x]$ , with a Dirac model, atomic densities calculated by DFT and separate core/valence densities.

		2D molecules from QM7			QM2D		
		$\overline{M}$	MAE	RMSE	$\overline{M}$	MAE	RMSE
Coulomb Matrix		N/A	$6.7 \pm 2.8$	$14.8 \pm 12.2$	N/A	$2.4 \pm 0.1$	$5.4 \pm 2.5$
Fourier	Dirac + Core/Valence	$73 \pm 27$	$6.7 \pm 0.7$	$8.5 \pm 0.9$	$244 \pm 52$	$5.3 \pm 0.2$	$7.2 \pm 0.4$
Wavelet	Dirac + Core/Valence	$38 \pm 13$	$6.9 \pm 0.6$	$9.1 \pm 0.8$	$46 \pm 4$	$5.4 \pm 0.1$	$7.1 \pm 0.3$
Scattering	Dirac	$43 \pm 32$	$15.9 \pm 1.7$	$23.9 \pm 7.2$	$262 \pm 81$	$9.2 \pm 0.1$	$11.7 \pm 0.1$
	Atomic	$99 \pm 40$	$4.0 \pm 0.5$	$5.2 \pm 0.6$	$299 \pm 56$	$2.7 \pm 0.0$	$3.8 \pm 0.2$
	Dirac + Atomic	$99 \pm 35$	$4.1 \pm 0.3$	$5.7 \pm 0.6$	$373 \pm 76$	$2.3 \pm 0.1$	$3.4 \pm 0.3$
	Core/Valence	$107 \pm 41$	$3.2 \pm 0.1$	$4.5 \pm 0.2$	$468 \pm 108$	$1.6 \pm 0.1$	$2.6 \pm 0.5$
	Dirac + Core/Valence	$97 \pm 45$	$3.5 \pm 0.2$	$5.0 \pm 0.6$	$450 \pm 91$	$1.6 \pm 0.0$	$2.5 \pm 0.4$

of the QM7 molecular database [25]. We also created a second database of 4357 strictly planar molecules, which we denote QM2D. Both databases consist of a set of organic molecules composed of Hydrogen, Carbon, Nitrogen, Oxygen, Sulfur and additionally Chlorine in the case of QM2D. The molecules featured in these databases cover a large spectrum of representative organic groups typically found in chemical compound space.

To evaluate the precision of each regression algorithm, each data set is broken into five representative folds, and all tests are performed using five fold cross validation as described in [25]. We reserve four folds for training and model selection, and the fifth fold for testing. We do so for each of the five possible permutations, and report average regression errors over the five test folds with their standard deviation. We compute both a mean absolute error (MAE) which is the average of the absolute value error over the testing fold, and the root mean-square error (RMSE) which is the square root of the average squared error.

For the Coulomb matrix kernel regression described in section 3.1, we use a collection of eight Coulomb matrices per molecule, as in [25]. The width  $\sigma$  of the kernel (6) and the ridge regression parameter  $\lambda$  in (5) are selected by cross validation, according to the algorithm described in [25]. The algorithm was validated by recovering the numerical precision given in [25] over the full QM7 database which includes 7165 molecules. In these experiments, we restrict the training database to a subset of the 454 planar molecules in QM7. Coulomb regression errors reported in table 1 are thus larger than in [25].

Sparse  $M$ -term regressions are computed in Fourier, wavelet and scattering dictionaries  $\Phi(x) = (\phi_k(x))_k = \Theta\rho[x]$ , using the orthogonal least-square

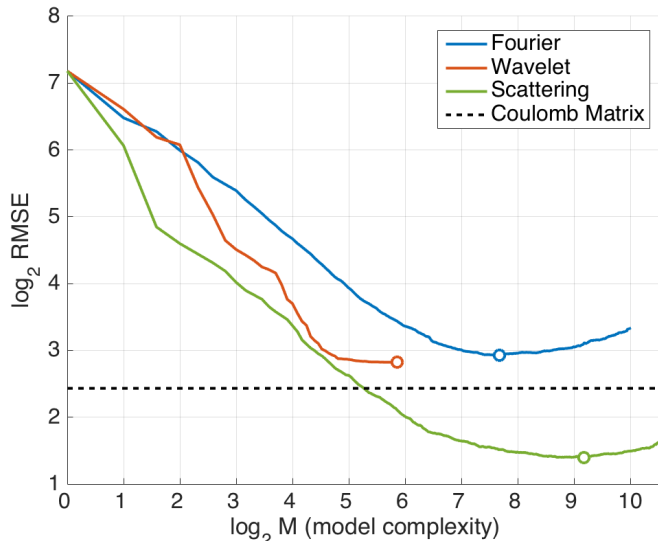


Figure 4:  $\log_2$  RMSE of the root mean square errors on the QM2D database of 4357 molecules, as a function of  $\log_2 M$ , where  $M$  is the number of regression terms. Coulomb is the black dashed line, Fourier is blue, wavelet is orange, and scattering is green. The circle indicates the optimal value of  $M$ .

regression algorithm described in section 3.2:

$$\tilde{f}(x) = \sum_{m=1}^M w_{k_m} \phi_{k_m}(x). \quad (16)$$

Figure 4 compares the value of the RMSE error as a function of the dimensionality  $M$  of the regression model, for each dictionary. In each case, the electronic density  $\rho$  is computed with (9), for core/valence densities  $\rho[z_k]$  computed by DFT as well as the Dirac density. Results show that the RMSE error is similar for the Fourier dictionary and the wavelet dictionary, although the wavelet dictionary needs significantly fewer terms to achieve the same minimum.

The regression error can be decomposed into a bias error due to the inability to precisely approximate  $f(x)$  from a linear expansion in the dictionary  $\Phi(x)$ , plus a variance term due to errors when optimizing the weights  $w_k$  from a limited training set. For the Fourier and wavelet dictionaries, observe that the error obtained on the planar molecules from the QM7 database of 454 molecules is only about 25% larger than the error on the QM2D database of 4357 molecules. On QM2D, it is also significantly bigger than the error obtained by Coulomb kernel regressions, which saw a drastic reduction in regression error when going from the smaller to the larger database. The fact that the overall error for Fourier and wavelet dictionaries is not significantly reduced when increasing

the database size by a factor of 10 indicates that the bias error dominates the variance error. It shows that the dictionary  $\Phi(x)$  must be complemented by more invariants to define a better approximation space.

Scattering regressions improve wavelet regressions by adding second order invariants. When the database size increases from 454 to 4357 molecules the scattering error decreases by approximately 50%, and is smaller than the Coulomb kernel regression error. The bias term has been reduced to match the variance term, which gets smaller when increasing the database size. With separated valence and core electronic densities, table 1 shows that the RMSE error of a scattering regression is 2.6 kcal/mol. Observe also that the MAE of the core/valence scattering regression is below 2.0 kcal/mol on the larger QM2D database, relative to the DFT energies on which the regression was trained. The consensus is that DFT has a hard time getting below 2 – 3 kcal/mol in MAE [28], and these errors correspond to very recent methods. Thus if the molecular energies were experimental and the scattering regression performed similarly, scattering regressions would be in the same range of errors as DFT on the QM2D database, which is promising.

Table 1 additionally indicates that the standard deviation of the scattering error is smaller than the standard deviation of the Coulomb matrix error. Furthermore the largest scattering errors are significantly smaller than the largest Coulomb matrix errors. The five largest Coulomb matrix regression errors on individual molecules from QM2D are 224, 185, 83, 70, and 53 (all in kcal/mol), whereas the five largest scattering errors are 62, 47, 40, 27, and 26 kcal/mol. These larger errors may result from Coulomb matrix instabilities, which originate from the fact that unsorted Coulomb matrices are not invariant to permutations; see the end of section 3.1 for a more detailed discussion.

Increasing the model dimension  $M$  increases the estimation variance but reduces the bias. The optimal choice of  $M$  results from a bias-variance trade-off, and it is estimated from the training data. Rather than estimate the optimal value of  $M$  via four fold cross validation on the training data, we apply a bagging algorithm to learn multiple models, each with their own model dimension, which are then averaged together to reduce the variance error. Each iteration of the bagging algorithm uniformly randomly selects  $\beta\%$  ( $0 < \beta < 100$ ) of the training data to train the model using the orthogonal least square algorithm, up to a large value  $M_0$  for the model dimension. The algorithm then selects a model dimension  $\bar{M} \leq M_0$  which minimizes the MAE or the RMSE on the remaining  $(100 - \beta)\%$  of the training data. The resulting  $\bar{M}$ -term regression is then computed on the test data. The procedure is repeated  $X$  times, and the regressions on the test data are averaged together to give the final regressed energies. In numerical experiments  $\beta = 90$  for the 454 nearly planar molecules from QM7 while  $\beta = 80$  for the larger QM2D data set; the number of bags is  $X = 10$  for both data sets. Table 1 reports the mean value of  $\bar{M}$  over the 10 bags, for the Fourier, wavelet and scattering dictionaries, as well as the corresponding mean absolute error (MAE) and root-mean-square error (RMSE), with the standard deviation over the five folds.

For a scattering transform, the model dimension  $\bar{M}$  is approximately 7.5

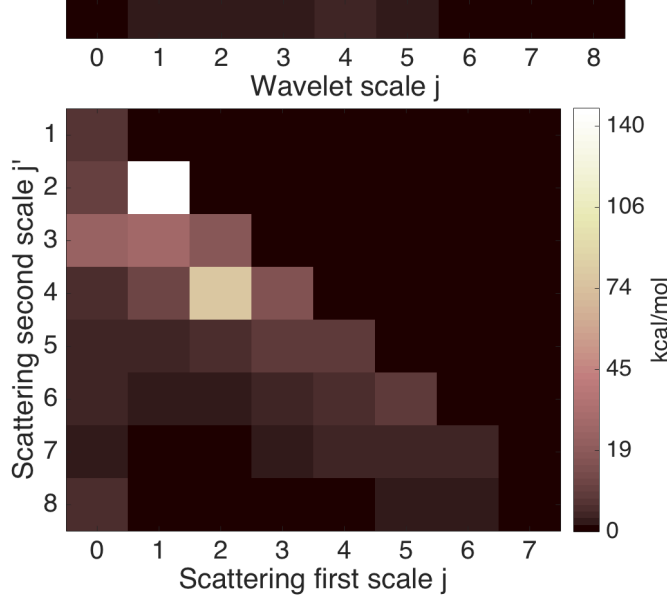


Figure 5: The average scattering weights  $\mathbb{E}_l \left( \frac{1}{\sqrt{n}} |\tilde{w}_k^l| \right)$  aggregated by scale. Lighter boxes indicate large amplitudes, darker boxes are small amplitudes. The upper row corresponds to the weights of wavelet coefficients  $\|\rho * \psi_{j,\cdot}\|_p^p$ , while the lower matrix shows the weights of scattering coefficients  $\frac{1}{2} \sum_{\varepsilon=-1,1} \|\rho * \psi_{j,\cdot} * \psi_{j',\varepsilon\theta'+\cdot}\|_p^p$  for  $j < j'$ .

times the number of parameters of a molecule. Indeed, each atom is specified by 3 variables, its two-dimensional position and its charge, so a molecule of 20 atoms has 60 free variables. The dominant scales of the wavelets selected by the orthogonal least square regression go from a small scale, localized around the center location of each atom, up to a large scale on the order of the diameter of the molecule. Scales beyond the diameter of the molecule are used sparingly. It is thus sufficient in the training phase to compute second order scattering interaction terms at the corresponding scales  $2^j$  and  $2^{j'}$ , which limits computations. In the testing phase, only the  $\bar{M}$  scattering paths used in the regression need be computed for new configurations, thus further limiting computations.

We further analyze the distribution of scattering coefficients used in the regression by computing the expected value of the squared amplitudes of the weights  $(\tilde{w}_{k_m})_{m \leq M}$  for the orthonormal scattering dictionary  $(\phi_{k_m}^m)_{m \leq M}$  (section 3.2), over the larger QM2D database. More precisely, a scattering regression model (8) with  $M = 2^9$  nonzero weights was trained from 80% of the QM2D database, uniformly randomly selected. The value  $M = 2^9$  was selected based on fig. 4, which indicates it is approximately the optimal value of  $M$  for scatter-

ing regressions on the QM2D database. The mean squared amplitude of each weight  $\tilde{w}_{k_m}$  over the sub-database  $\{x_i\}_{i \leq n}$  is computed as:

$$\mathbb{E}_x(|\tilde{w}_{k_m} \phi_{k_m}^m(x)|^2) = \frac{1}{n} \sum_{i=1}^n |\tilde{w}_{k_m} \phi_{k_m}^m(x_i)|^2 = \frac{1}{n} |\tilde{w}_{k_m}|^2.$$

The process was repeated  $10^3$  times over different draws of the training set, yielding a set of weights  $(\tilde{w}_k^l)_{k,l}$ , where  $k$  indexes the scattering coefficient and  $l = 1, \dots, 10^3$  indexes the draw. If on the  $l^{\text{th}}$  draw a scattering coefficient  $\phi_k$  is not selected within the first  $2^9$  iterations of the orthogonal least square algorithm, the corresponding weight is set to zero,  $\tilde{w}_k^l = 0$ . The resulting  $10^3$  root mean squared amplitudes for each  $k$  are averaged over the draws,

$$\mathbb{E}_l \left( \frac{1}{\sqrt{n}} |\tilde{w}_k^l| \right) = 10^{-3} \sum_{l=1}^{10^3} \frac{1}{\sqrt{n}} |\tilde{w}_k^l|. \quad (17)$$

Figure 5 displays the values (17) summed according to their scale, meaning that they were aggregated over the non-scale scattering parameters corresponding to the density (Dirac, core, valence), the norm ( $\mathbf{L}^1$ ,  $\mathbf{L}^2$ ), and the angle  $\theta'$  for second order coefficients. From this figure we observe:

1. The dominant weights are on second layer scattering coefficients, giving further numerical validation to their importance. Amongst them, the weights corresponding to  $(j, j') = (1, 2)$  have the largest value by a significant margin. Further numerical investigation shows that the first scattering coefficient selected in all  $10^3$  iterations is  $\|\rho_{\text{val}}\|_1$  (not shown in fig. 5) and it's corresponding weight is approximately 1475 kcal/mol in amplitude, which is the order of magnitude of the energy of a single molecule. The second coefficient selected, however, is always  $\|\rho_{\text{val}} * \psi_{1,\cdot} \|\psi_{2,0+}\|_1$ , with corresponding mean weight  $\mathbb{E}_l \left( \frac{1}{\sqrt{n}} |\tilde{w}_k^l| \right) \approx 129$  kcal/mol, which constitutes approximately 90% of the energy of all second order weights corresponding to scales  $(j, j') = (1, 2)$ .
2. The majority of the energy in the second layer coefficients  $\frac{1}{2} \sum_{\varepsilon=-1,1} \|\rho * \psi_{j,\cdot} \|\psi_{j',\varepsilon\theta'+\cdot}\|_p^p$  is concentrated along the band of scales  $j < j'$  with  $|j - j'| \leq 3$ . It can be interpreted physically as an interaction between two scales, for example between micro- and meso-scale interactions or meso- and macro-scale interactions. This type of coupling property was also observed for multifractal stochastic processes in [12]. Practically, it means that to regress the majority of the energy, only second order scattering coefficients within the band  $|j - j'| \leq 3$  need to be computed.
3. Wavelet coefficients  $\|\rho * \psi_{j,\cdot}\|_p^p$  contain significantly less energy than second order scattering coefficients. Amongst these first order coefficients, micro- and meso-scales ( $j = 0, \dots, 5$ ) are used more than large scale wavelets ( $j \geq 6$ ).

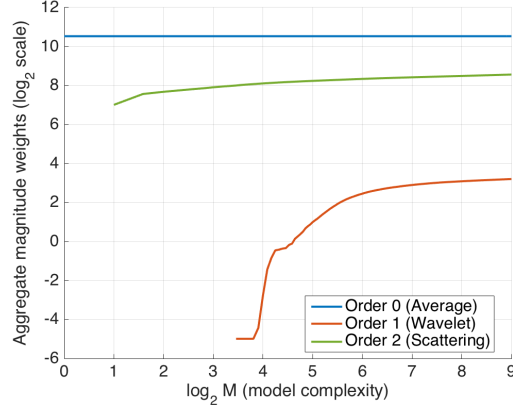
Building upon the first remark, we observe that the first five scattering coefficients are constant across all  $10^3$  draws of the training set. They are:

1.  $\|\rho_{\text{val}}\|_1$
2.  $\|\rho_{\text{val}} * \psi_{1,\cdot} | * \psi_{2,0+\cdot}\|_1$
3.  $\frac{1}{2} \sum_{\varepsilon=-1,1} \|\rho_{\text{val}} * \psi_{2,\cdot} | * \psi_{4,\varepsilon \frac{5\pi}{16}+\cdot}\|_2^2$
4.  $\|\rho_{\text{val}} * \psi_{1,\cdot} | * \psi_{3,\frac{\pi}{2}+\cdot}\|_1$
5.  $\frac{1}{2} \sum_{\varepsilon=-1,1} \|\rho_{\text{val}} * \psi_{0,\cdot} | * \psi_{3,\varepsilon \frac{3\pi}{16}+\cdot}\|_1$

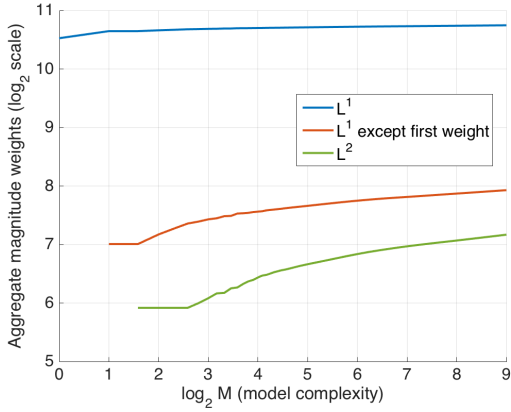
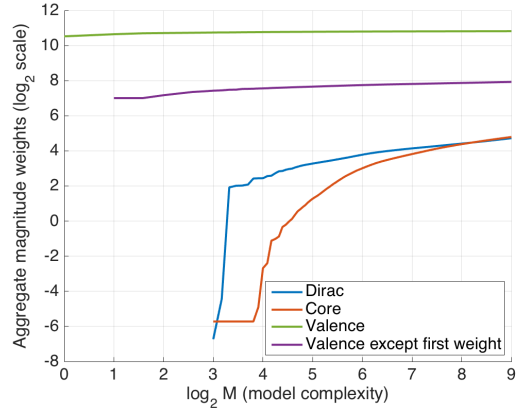
Observe that after the first coefficient, the next four coefficients are second order scattering coefficients that all lie within the band  $|j - j'| \leq 3$ . Furthermore, amongst the first five coefficients, all utilize the valence density and four out of five are  $\mathbf{L}^1$  norms. These five coefficients serve as a microcosm for trends observed amongst the first  $2^9$  selected scattering coefficients, some of which were described above in reference to fig. 5, while other trends are described below and in fig. 6. Given that these five coefficients are universally selected global invariants, it is an interesting open question, particularly for the second order terms, to understand how these coefficients relate to the chemical properties of the molecules in the database. After the fifth selected term, the orthogonal least square algorithm branches out. There are four possibilities for the sixth coefficient, although all are  $\mathbf{L}^1$  norm second order coefficients. By the seventh coefficient, both  $\mathbf{L}^1$  and  $\mathbf{L}^2$  second order coefficients are possible. An order one wavelet coefficient is selected, at the earliest, as the 11<sup>th</sup> coefficient.

Average scattering weights  $\mathbb{E}_l \left( \frac{1}{\sqrt{n}} |\tilde{w}_k^l| \right)$  were also summed according to other parameter dimensions in addition to their scale. In Figure 6(a) they are organized according to the order of the corresponding scattering coefficient, by aggregating along  $k$  the values  $\mathbb{E}_l \left( \frac{1}{\sqrt{n}} |\tilde{w}_k^l| \right)$  which correspond to order zero coefficients of the form  $\|\rho\|_1$ , order one coefficients of the form  $\|\rho * \psi_{j,\cdot}\|_p^p$ , and order two coefficients of the form  $\frac{1}{2} \sum_{\varepsilon=-1,1} \|\rho * \psi_{j,\cdot} | * \psi_{j',\varepsilon\theta'+\cdot}\|_p^p$ . The summed magnitude of each type of coefficient is plotted as a function of the model dimension  $M$ . As expected from the previous discussion, the plot indicates that an order zero coefficient is selected first, which is in fact  $\|\rho_{\text{val}}\|_1$ , and that the magnitude of its corresponding weight dominates the magnitudes of all subsequent weights. Such a coefficient captures the total valence electronic charge of each molecule. Second order scattering terms in turn dominate first order wavelet terms, indicating once again their usefulness.

Figure 6(b) plots the magnitudes of  $\mathbf{L}^1$  and  $\mathbf{L}^2$  aggregated scattering weights. Recall that  $\mathbf{L}^1$  coefficients scale with the number of bonds, while  $\mathbf{L}^2$  coefficients incorporate quadratic behavior resulting from Coulomb interactions. Including the first weight for the coefficient  $\|\rho_{\text{val}}\|_1$  shows that  $\mathbf{L}^1$  energies dominate  $\mathbf{L}^2$  energies. However, when this weight is removed, Figure 6(b) indicates that the two types of coefficients are more balanced, with  $\mathbf{L}^1$  weights accounting for approximately twice the energy as  $\mathbf{L}^2$  weights.



(a) Order zero, one, and two average scattering weights.

(b) L<sup>1</sup> and L<sup>2</sup> average scattering weights.

(c) Dirac, core, and valence average scattering weights.

Figure 6: Comparison of the average scattering weights  $\mathbb{E}_l \left( \frac{1}{\sqrt{n}} |\tilde{w}_k^l| \right)$  for three different categories of the coefficients: the order of the coefficient (zero, one, or two), the norm of the coefficient (L<sup>1</sup> or L<sup>2</sup>), and the type of density (Dirac, core, valence).

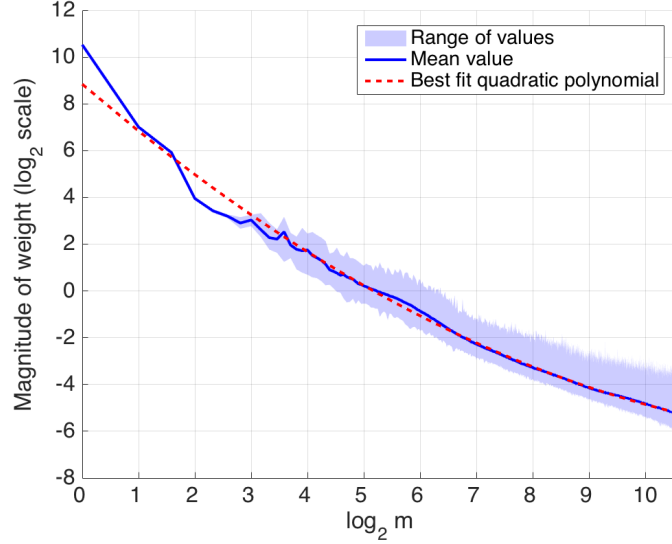


Figure 7: Decay of the scattering weights’ magnitude  $\frac{1}{\sqrt{n}}|\tilde{w}_{k_m}^l|$  as a function of  $m$ . The solid line is  $\mathbb{E}_l\left(\frac{1}{\sqrt{n}}|\tilde{w}_{k_m}^l|\right)$ , while the upper bound of the shaded region is  $\max_l\left(\frac{1}{\sqrt{n}}|\tilde{w}_{k_m}^l|\right)$  and lower bound is  $\min_l\left(\frac{1}{\sqrt{n}}|\tilde{w}_{k_m}^l|\right)$ . The red dashed curve is the quadratic polynomial that best fits  $\mathbb{E}_l\left(\frac{1}{\sqrt{n}}|\tilde{w}_{k_m}^l|\right)$  on a  $\log_2 - \log_2$  scale.

The precision of the regression also depends upon the electronic density models  $\rho[z_k]$  used to compute the non-interacting density  $\rho[x] = \sum_k \rho[z_k](u - r_k)$ . Table 1 shows that the error obtained with a point charge Dirac density is more than three times as big as the error obtained with the electronic density of isolated atoms, computed by DFT. The density model which separates valence and core electronic densities further reduces the error by more than 30%. This model multiplies by two the number of invariants of each dictionary since invariants are computed separately for the core and valence densities. The primary factor in the improvement is the separated valence density. Indeed, Figure 6(c) shows that the energy of valence coefficients dominates the energy of core and Dirac density weights, even if the weight corresponding to  $\|\rho_{\text{val}}\|_1$  is removed. This phenomena is chemically intuitive, since differences between molecules result primarily from the interactions of valence electrons of constituent atoms. From table 1 we also observe that the addition of the Dirac density, theoretically used to learn the nuclei Coulomb interactions (section 8), to either the atomic density or core/valence densities yields only a small improvement in the numerical precision. It can thus be omitted in computations.

Finally, we study the decay of the weights’ magnitude  $|\tilde{w}_{k_m}^l|$  as a function of  $m$ , which by (7) determines the rate of convergence of  $\tilde{f}$  to  $f$  on the training

set. We extend the numerical experiment that generated figs. 5 and 6 by computing the weights  $\tilde{w}_{k_m}^l$  up to  $m = 3 \cdot 2^9$  (the same maximum model dimension  $M$  in fig. 4). In fig. 7 we plot  $\mathbb{E}_l \left( \frac{1}{\sqrt{n}} |\tilde{w}_{k_m}^l| \right)$  as well as  $\max_l \left( \frac{1}{\sqrt{n}} |\tilde{w}_{k_m}^l| \right)$  and  $\min_l \left( \frac{1}{\sqrt{n}} |\tilde{w}_{k_m}^l| \right)$  as a function of  $m$ . From the figure we observe that on the  $\log_2 - \log_2$  scale, the weights decay similarly to the decreasing part of a convex quadratic polynomial. This implies:

$$\mathbb{E}_l \left( \frac{1}{\sqrt{n}} |\tilde{w}_{k_m}^l| \right) \approx 2^c m^{a \log_2 m + b}, \quad a > 0, \quad b < 0, \quad 1 \leq m \leq 3 \cdot 2^9. \quad (18)$$

Equation (18) shows that  $\mathbb{E}_l \left( \frac{1}{\sqrt{n}} |\tilde{w}_{k_m}^l| \right)$  satisfies a variable power law  $C|m|^{-\alpha(m)}$ , where  $\alpha(m)$  decreases linearly as a function of  $\log_2 m$ . For the polynomial plotted in fig. 7,  $a \approx 0.07$  and  $b \approx -2.1$  and the polynomial is given by  $P(x) = ax^2 + bx + c$ . Thus the power  $\alpha(m)$  decreases from approximately 2.1 at  $m = 1$ , to 1.4 at  $m = 2^9$  (the approximate best value of  $M$  from table 1 and fig. 4), to 1.3 at  $m = 3 \cdot 2^9$ . While the initial power law gives a fast rate of convergence, it slows as  $m$  gets larger thereby giving diminishing returns for  $\tilde{f}$  as the orthogonal least square algorithm progresses. Figure 4 indicates that the diminishing improvement in the bias error of the model is overtaken by the increasing variance error at approximately  $m = 2^9$ .

## 8 Regression of Coulomb Energy Functionals

We study the regression of Coulomb potential energies with Fourier and wavelet invariant dictionaries. Let us first relate Coulomb energy terms to the quantum energy of a molecule.

The Kohn-Sham approach to density functional theory decomposes the energy as a sum of four terms in (4). The ground state energy  $f(x)$  is obtained by adding the nuclei-nuclei Coulomb potential energy in (3), which can be rewritten:

$$f(x) = T(\rho_0) + \frac{1}{2} U(\rho_n - \rho_0) + E_{xc}(\rho_0),$$

where  $\rho_0$  is the ground state electronic density and  $\rho_n = \sum_k z_k \delta(u - r_k)$  is the point charges of the nuclei. The first term  $T(\rho_0)$  is the Kinetic energy and  $E_{xc}(\rho_0)$  is the exchange correlation energy. The Coulomb potential energy of the electronic density and the nuclei charges are regrouped in

$$U(\rho) = \text{p.v.} \int_{\mathbb{R}^3} \int_{\mathbb{R}^3} \frac{\rho(u) \rho(v)}{|u - v|} du dv, \quad (19)$$

evaluated for the overall charge density  $\rho = \rho_n - \rho_0$ . Whereas the ground state electronic density  $\rho_0$  is Lipschitz with fast decay, the nuclei density  $\rho_n$  is a sum of Diracs. The Coulomb integral is defined as the Cauchy principal value integral to handle the singularity of the Coulomb kernel  $|u|^{-1}$  for point charges. To

simplify notations, we omit the p.v. notation, but all Coulomb energy integrals are defined in that sense.

The exchange correlation energy is a complicated term which makes the mathematical analysis of solutions particularly difficult. In the following, we concentrate on the Coulomb energy potential  $U(\rho)$ . Section 8.1 proves that the Coulomb energy potential is linearly regressed with an error  $O(\epsilon^{1-\delta})$  with  $O(\epsilon^{-2})$  Fourier invariants calculated from  $\rho$ , for arbitrary  $\delta > 0$ . Section 8.2 proves that a wavelet invariant dictionary produces a regression error  $O(\epsilon)$  with only  $O(|\log \epsilon|)$  terms.

### 8.1 Fourier Invariant Regression

The Coulomb potential energy  $U(\rho)$  is invariant to isometries. We prove that it can be linearly regressed over the quadratic Fourier invariants introduced in section 5:

$$\|\hat{\rho}_\alpha\|_2^2 = \int_{S^2} |\hat{\rho}(\alpha\eta)|^2 d\eta.$$

The Coulomb energy (19) can be written as a convolution

$$U(\rho) = \text{p.v.} \int_{\mathbb{R}^3} \bar{\rho} * \rho(u) |u|^{-1} du,$$

with  $\bar{\rho}(u) = \rho(-u)$ . Since the Fourier transform of  $|u|^{-1}$  is  $4\pi|\omega|^{-2}$ , the Parseval formula gives

$$U(\rho) = \frac{4\pi}{(2\pi)^3} \int_{\mathbb{R}^3} \frac{|\hat{\rho}(\omega)|^2}{|\omega|^2} d\omega. \quad (20)$$

Let  $\delta > 0$ . The following theorem gives a regression of  $U(\rho)$  using  $\epsilon^{-2}$  quadratic Fourier invariants  $\|\hat{\rho}_\alpha\|_2^2$  sampled on an  $\epsilon$ -grid of  $[\epsilon, \epsilon^{-1}]$ . It proves that the regression error is  $O(\epsilon^{1-\delta})$ . Like  $\rho_n - \rho_0$ ,  $\rho$  is a sum of a Lipschitz function with fast decay and a finite number of point charges.

**Theorem 1.** *If  $\rho$  is a sum of a Lipschitz function in  $\mathbf{L}^1(\mathbb{R}^3)$  with exponential decay and a finite number of point charges, then for any  $0 < \epsilon < 1$  and  $0 < \delta < 1$ ,*

$$U(\rho) = \frac{\epsilon}{4\pi^2} \left( \|\hat{\rho}_\epsilon\|_2^2 + 2 \sum_{k=2}^{\epsilon^{-2}-1} \|\hat{\rho}_{k\epsilon}\|_2^2 + \|\hat{\rho}_{\epsilon^{-1}}\|_2^2 \right) + O(\epsilon^{1-\delta}), \quad \text{as } \epsilon \rightarrow 0. \quad (21)$$

*Proof.* Since  $\|\hat{\rho}_\alpha\|_2^2 = \int_{S^2} |\hat{\rho}(\alpha\eta)|^2 d\eta$  it results from (20) that

$$\begin{aligned} U(\rho) &= \frac{1}{2\pi^2} \int_0^\infty \frac{1}{\alpha^2} \int_{S_\alpha^2} |\hat{\rho}(\bar{\eta})|^2 d\bar{\eta} d\alpha, \\ &= \frac{1}{2\pi^2} \int_0^\infty \frac{1}{\alpha^2} \cdot \alpha^2 \int_{S^2} |\hat{\rho}(\alpha\eta)|^2 d\eta d\alpha = \frac{1}{2\pi^2} \int_0^\infty \|\hat{\rho}_\alpha\|_2^2 d\alpha, \end{aligned}$$

where  $S_\alpha^2 \subset \mathbb{R}^3$  is the sphere of radius  $\alpha$ . The following lemma gives a low and high frequency cut of this integral to obtain an error  $O(\epsilon^{1-\delta})$ .

**Lemma 2.** *Under the hypotheses of theorem 1,*

$$\int_{|\omega| < \epsilon} \frac{|\hat{\rho}(\omega)|^2}{|\omega|^2} d\omega = O(\epsilon),$$

and for any  $0 < \delta < 1$ ,

$$\int_{|\omega| > \epsilon^{-1}} \frac{|\hat{\rho}(\omega)|^2}{|\omega|^2} d\omega = O(\epsilon^{1-\delta}).$$

It results from this lemma that

$$U(\rho) = \frac{1}{2\pi^2} \int_{\epsilon}^{\epsilon^{-1}} \|\hat{\rho}_{\alpha}\|_2^2 d\alpha + O(\epsilon^{1-\delta}). \quad (22)$$

This second lemma provides a Riemann sum approximation of this integral using the trapezoid rule.

**Lemma 3.** *Under the hypotheses of theorem 1,*

$$\int_{\epsilon}^{\epsilon^{-1}} \|\hat{\rho}_{\alpha}\|_2^2 d\alpha = \frac{\epsilon}{2} \left( \|\hat{\rho}_{\epsilon}\|_2^2 + 2 \sum_{k=2}^{\epsilon^{-2}-1} \|\hat{\rho}_{k\epsilon}\|_2^2 + \|\hat{\rho}_{\epsilon^{-1}}\|_2^2 \right) + O(\epsilon). \quad (23)$$

Inserting (23) in (22) proves (21). The proofs of lemmas 2 and 3 are given in appendices B.1 and B.2, respectively.  $\square$

Since  $\delta$  can be made arbitrarily small, theorem 1 proves, for all practical purposes, that Fourier regressions can approximate  $U(\rho)$  to accuracy  $O(\epsilon)$  utilizing  $O(\epsilon^{-2})$  invariants. Lemma 3 can be improved by utilizing higher order Newton-Cotes numerical integration schemes [26], in which case one can show that for an arbitrary  $\delta' > 0$  independent of  $\delta$ , there exists  $O(\epsilon^{-(1+\delta')})$  quadratic Fourier invariants that regress  $U(\rho)$  to accuracy  $O(\epsilon^{1-\delta})$ ; some additional remarks along these lines are given in appendix B.2. Furthermore, the assumptions on  $\rho$  are physically valid. Indeed, it is reasonable to assume  $\rho_0$  is Lipschitz, see for example [20], and it is known [35] that the electronic density  $\rho_0(u)$  decays exponentially fast as  $|u| \rightarrow \infty$ .

## 8.2 Wavelet Invariant Regression

A Coulomb potential energy is computed with the singular convolution kernel  $|u|^{-1}$ . The Fourier spectrum  $4\pi|\omega|^{-2}$  is singular at  $\omega = 0$  and has a slow decay. Such homogeneous singular operators are better represented with wavelet transforms [15, 33, 34, 30]. The following theorem proves that Coulomb potentials have a much more sparse regression over quadratic wavelet invariants,

$$\|\rho * \psi_{j,\cdot}\|_2^2 = \int_{\mathbb{R}^3 \times [0,\pi]^2} |\rho * \psi_{j,\theta}(u)|^2 du d\theta,$$

than over Fourier invariants.

**Theorem 4.** *Suppose  $\psi$  has compactly supported Fourier transform and satisfies for  $\omega \neq 0$ ,*

$$\sum_{j \in \mathbb{Z}} 2^{2j} \int_{[0, \pi]^2} |\widehat{\psi}(2^j r_\theta^{-1} \omega)|^2 d\theta = |\omega|^{-2}. \quad (24)$$

*If  $\rho$  is the sum of a Lipschitz function in  $\mathbf{L}^1(\mathbb{R}^3)$  and a finite number of point charges, then:*

$$U(\rho) = 4\pi \sum_{j=2 \log_2 \epsilon}^{-\log_2 \epsilon} 2^{2j} \|\rho * \psi_{j, \cdot}\|_2^2 + O(\epsilon), \quad \text{as } \epsilon \rightarrow 0. \quad (25)$$

*Proof.* Since

$$U(\rho) = \frac{4\pi}{(2\pi)^3} \int_{\mathbb{R}^3} \frac{|\hat{\rho}(\omega)|^2}{|\omega|^2} d\omega,$$

inserting (24) gives

$$U(\rho) = \frac{4\pi}{(2\pi)^3} \sum_{j \in \mathbb{Z}} 2^{2j} \int_{[0, \pi]^2} \int_{\mathbb{R}^3} |\widehat{\psi}_{j, \theta}(\omega)|^2 |\hat{\rho}(\omega)|^2 d\omega d\theta.$$

Applying the Plancherel formula proves that

$$U(\rho) = 4\pi \sum_{j \in \mathbb{Z}} 2^{2j} \|\rho * \psi_{j, \cdot}\|_2^2. \quad (26)$$

The following lemma proves that the infinite sum over  $j$  can be truncated with an  $O(\epsilon)$  error; its proof is in appendix B.3.

**Lemma 5.** *Under the hypotheses of theorem 4,*

$$\sum_{j=-\infty}^{2 \log_2 \epsilon} 2^{2j} \|\rho * \psi_{j, \cdot}\|_2^2 = O(\epsilon), \quad (27)$$

and

$$\sum_{j=-\log_2 \epsilon}^{+\infty} 2^{2j} \|\rho * \psi_{j, \cdot}\|_2^2 = O(\epsilon). \quad (28)$$

Inserting (27) and (28) in (26) proves (25).  $\square$

This theorem proves that Coulomb potential energy can be regressed to  $O(\epsilon)$  error with  $3|\log_2 \epsilon| = O(|\log \epsilon|)$  wavelet invariants, as opposed to  $O(\epsilon^{-2})$  Fourier invariants. Similarly to multipole approximations of Coulomb potentials [23, 22], the wavelet transform regroups Coulomb interactions at distances of the order of  $2^j$ , which gives an efficient regression formula.

The wavelet condition (24) is satisfied if  $\widehat{\psi}(\omega) = |\omega|^{-1} \widehat{\psi}^0(\omega)$  where  $\widehat{\psi}^0(\omega)$  satisfies the exact Littlewood-Paley condition for all  $\omega \neq 0$ :

$$\sum_{j \in \mathbb{Z}} \int_{[0, \pi]^2} |\widehat{\psi}^0(2^j r_\theta^{-1} \omega)|^2 d\theta = 1.$$

In the last two sections, we computed  $U(\rho)$  by supposing that  $\rho$  is known. Given the molecular state  $x = \{z_k, r_k\}_k$ , the pointwise nuclear charge  $\rho_n(u) = \sum_k z_k \delta(u - r_k)$  is known, but the ground state electronic density  $\rho_0(u)$  is unknown. The non-interacting electronic densities  $\rho[x]$  are crude approximations of  $\rho_0$ . One may however approximate  $\rho_0$  through deformations of  $\rho[x]$ . Since wavelet transforms are Lipschitz continuous to deformations, adjusting the linear regression coefficients in (25) can partly take into account the electronic density errors. Such adjustments are more unstable with Fourier invariant regressions, because of the Fourier instabilities to deformations at high frequencies.

## 9 Conclusion

We introduced a multiscale dictionary of invariants to compute sparse regressions of quantum molecular energies. We proved that Coulomb potential energies are regressed with few wavelet transform invariants, but these invariants do not have enough flexibility to accurately regress quantum molecular energies. Wavelet invariants are complemented by multiscale scattering invariants providing higher order interaction terms, which improve energy regressions.

Numerical regression errors over two databases of planar molecules are of the order of DFT errors, but further numerical experiments over larger databases of three dimensional molecules are needed to evaluate the range of validity of these quantum energy regressions. A priori there is no mathematical difficulty in working with three dimensional molecules, and indeed all of the mathematical analysis is carried out over  $\mathbb{R}^3$ . Numerically, ongoing work includes the development of computational and memory efficient three dimensional wavelet filters, done in part by leveraging the symmetries described in appendix A. Already though these numerical results over planar molecules are opening mathematical questions to relate more precisely second order scattering coefficients to the properties of kinetic energy terms and exchange correlation energy terms of density functional theory.

Let us finally emphasize that scattering energy regressions rely on general invariance and stability properties, which are common to large classes of interacting many body problems. Multiscale scattering regressions may thus also apply to other many body problems, which exhibit complex multiscale behavior, such as in astronomy, atmospheric science, and fluid mechanics.

## A Wavelet Scattering Symmetries

We prove that second layer scattering terms  $\|\rho * \psi_{j,\cdot} * \psi_{j',\theta'+\cdot}\|_p^p$ , for  $p = 1, 2$ ,  $j, j' \in \mathbb{Z}$ , and  $\theta' \in [0, \pi]^2$ , in fact only depend on a one dimensional angle parameter as opposed to the two dimensional  $\theta'$ . In doing so, we give a more detailed explanation of the wavelet and scattering symmetries described in sections 6.1 and 6.2, and show how one might practically implement the scattering transform to take these symmetries into account.

To do so, we index rotations of the wavelet  $\psi$  by unit vectors  $\eta \in S^2$  as opposed to the Euler angle  $\theta$ . Recall  $\psi$  is assumed to have two symmetry properties: (i)  $\psi^*(u) = \psi(-u)$ , and (ii)  $\psi$  is symmetric about an axis  $\eta_0$ , meaning  $\psi(ru) = \psi(u)$  for any  $r \in \text{O}(3)$  that fixes  $\eta_0$ , i.e.,  $r\eta_0 = \eta_0$ . Define:

$$\psi_{j,r}(u) = 2^{-3j}\psi(2^{-j}r^{-1}u), \quad j \in \mathbb{Z}, r \in \text{O}(3),$$

and recall that  $\text{O}(3) = \text{SO}(3) \times \{I, -I\}$ . Since we exclusively consider the wavelet modulus transform, and since property (i) implies  $|\rho * \psi_{j,r}| = |\rho * \psi_{j,-r}|$ , we can restrict  $\psi_{j,r}$  to  $r \in \text{SO}(3)$ . Furthermore, let  $r_\eta \in \text{SO}(3)$  denote a rotation that moves  $\eta_0$  to  $\eta$ :

$$r_\eta \eta_0 = \eta. \quad (29)$$

The wavelet  $\psi_{j,r_\eta}$  is symmetric about  $\eta$ , and furthermore

$$\psi_{j,r_\eta} = \psi_{j,\tilde{r}_\eta}, \quad (30)$$

for any two rotations  $r_\eta, \tilde{r}_\eta \in \text{SO}(3)$  defined by (29). Therefore we can index the rotated wavelet by  $\eta \in S^2$ , and set:

$$\psi_{j,\eta}(u) = 2^{-3j}\psi(2^{-j}r_\eta^{-1}u), \quad j \in \mathbb{Z}, \eta \in S^2. \quad (31)$$

Second layer scattering terms are represented as follows. The second wavelet modulus transform is computed as:

$$|\rho * \psi_{j,\eta}| * \psi_{j',r_\eta\gamma}(u) = \left| \int_{\mathbb{R}^3} \rho(v) 2^{-3j} \psi(2^{-j}r_\eta^{-1}(\cdot - v)) dv \right| * \psi_{j',r_\eta\gamma}(u),$$

where  $j' \in \mathbb{Z}$  and  $\gamma \in S^2$ . Similar to the Euler angle presentation, the orientation of the second wavelet is decomposed as an increment of the first wavelet orientation. In this case, the axis  $\eta_0$  is first moved to  $\gamma$ , and then  $\gamma$  is moved to a new axis by the same rotation that moves  $\eta_0$  to  $\eta$ . Isometry invariant scattering coefficients are derived by integrating over  $\eta$  and  $u$ :

$$\|\rho * \psi_{j,\cdot} * \psi_{j',r_\cdot\gamma}\|_p^p = \int_{\mathbb{R}^3} \int_{S^2} |\rho * \psi_{j,\eta}| * \psi_{j',r_\eta\gamma}(u)|^p d\eta du.$$

In the vector presentation, second layer scattering coefficients are a priori indexed by  $j, j'$ , and  $\gamma \in S^2$ . We now show that they only depend on the one dimensional angle between  $\eta$  and  $r_\eta\gamma$ , as opposed to the two dimensional  $\gamma$ . First note that this angle is indeed fixed and is equal to  $\arccos(\eta_0 \cdot \gamma)$ , since  $\eta \cdot r_\eta\gamma = r_\eta^{-1}\eta \cdot \gamma = \eta_0 \cdot \gamma$ . Now let  $\delta \in S^2$  be a second vector such that  $\eta_0 \cdot \delta = \eta_0 \cdot \gamma$ , which implies that there exists a  $r_{\eta_0} \in \text{SO}(3)$  such that  $r_{\eta_0}\delta = \gamma$ . Therefore:

$$r_\gamma\eta_0 = r_{r_{\eta_0}\delta}\eta_0 = r_{\eta_0}\delta = r_{\eta_0}r_\delta\eta_0,$$

for any  $r_\gamma, r_\delta \in \text{SO}(3)$ . In particular, we can take  $r_\gamma = r_{\eta_0}r_\delta$ . This yields:

$$r_\eta\gamma = r_\eta r_\gamma\eta_0 = r_\eta r_{\eta_0}r_\delta\eta_0 = r_\eta r_{\eta_0}\delta.$$

But  $r_\eta r_{\eta_0} \eta_0 = \eta$ , which implies  $\tilde{r}_\eta = r_\eta r_{\eta_0}$ . Therefore  $r_\eta \gamma = \tilde{r}_\eta \delta$ , which completes the proof by (30).

The rotation  $r_\eta$  in (31) can be any rotation satisfying (29). In practice one can use the following construction. Let

$$\nu = \eta_0 \times \eta,$$

where  $\times$  denotes the usual cross product. Define the skew symmetric cross product matrix of  $\nu$  as:

$$[\nu]_\times = \begin{pmatrix} 0 & -\nu_3 & \nu_2 \\ \nu_3 & 0 & -\nu_1 \\ -\nu_2 & \nu_1 & 0 \end{pmatrix},$$

where  $\nu = (\nu_1, \nu_2, \nu_3)$ . One can then take  $r_\eta$  to be:

$$r_\eta = \begin{cases} I, & \eta = \eta_0, \\ I + 2[\nu]_\times^2, & \eta = -\eta_0, \\ I + [\nu]_\times + \frac{1 - \eta_0 \cdot \eta}{\|\nu\|^2} [\nu]_\times^2, & \text{otherwise.} \end{cases}$$

If one takes  $\eta_0 = (1, 0, 0)$ , then by the above proof, second layer terms are only distinguished by the value  $\eta_0 \cdot \gamma = \gamma_1$ , where  $\gamma = (\gamma_1, \gamma_2, \gamma_3)$ . Therefore one can parameterize the second layer with  $(j, j', t) \in \mathbb{Z} \times \mathbb{Z} \times [0, 1]$ , utilizing coefficients:

$$\|\rho * \psi_{j,\cdot} * \psi_{j',r,\gamma(t)}\|_p^p = \int_{\mathbb{R}^3} \int_{S^2} |\rho * \psi_{j,\eta}| * \psi_{j',r,\gamma(t)}(u)|^p d\eta du,$$

where  $\gamma(t) = (1 - t, \sqrt{t(2-t)}, 0)$ ,  $t \in [0, 1]$ .

## B Coulomb Regression Lemmas from Section 8

### B.1 Proof of lemma 2

Recall lemma 2 from section 8.1.

**Lemma 6** (Restatement of lemma 2). *Let  $\rho$  be the sum of a Lipschitz function in  $\mathbf{L}^1(\mathbb{R}^3)$  and a finite number of point charges. Then:*

1. *There exists a constant  $C$  such that for any  $\epsilon > 0$ ,*

$$\int_{|\omega| < \epsilon} \frac{|\hat{\rho}(\omega)|^2}{|\omega|^2} d\omega \leq C \cdot \epsilon. \quad (32)$$

2. *For each  $0 < \beta < 1$ , there exists a constant  $C$  such that for any  $0 < \epsilon < 1$ ,*

$$\int_{|\omega| > \epsilon^{-1}} \frac{|\hat{\rho}(\omega)|^2}{|\omega|^2} d\omega \leq C \cdot \epsilon^\beta. \quad (33)$$

*Proof of (32).* Since  $\rho \in \mathbf{L}^1(\mathbb{R}^3)$ , we have  $\hat{\rho} \in \mathbf{L}^\infty(\mathbb{R}^3)$  with  $\|\hat{\rho}\|_\infty \leq \|\rho\|_1$ . Using this fact with a change to spherical coordinates yields:

$$\begin{aligned} \int_{|\omega| < \epsilon} \frac{|\hat{\rho}(\omega)|^2}{|\omega|^2} d\omega &\leq \|\hat{\rho}\|_\infty^2 \int_{|\omega| < \epsilon} |\omega|^{-2} d\omega, \\ &\leq \|\rho\|_1^2 \int_0^{2\pi} \int_0^\pi \int_0^\epsilon \alpha^{-2} \cdot \alpha^2 \cdot \sin \vartheta d\alpha d\vartheta d\varphi, \\ &\leq C \cdot \|\rho\|_1^2 \cdot \epsilon. \end{aligned}$$

□

The proof of (33) is more delicate and will be broken into two cases. Recall that  $\rho = \rho_n - \rho_0$  where  $\rho_0 \in \mathbf{L}^1(\mathbb{R}^3)$  is Lipschitz, and  $\rho_n$  is the sum of a finite number of point charges. Thus:

$$\int_{|\omega| > \epsilon^{-1}} \frac{|\hat{\rho}(\omega)|^2}{|\omega|^2} d\omega = \int_{|\omega| > \epsilon^{-1}} \frac{|\hat{\rho}_n(\omega)|^2 + |\hat{\rho}_0(\omega)|^2 - \hat{\rho}_n(\omega)\hat{\rho}_0^*(\omega) - \hat{\rho}_n^*(\omega)\hat{\rho}_0(\omega)}{|\omega|^2} d\omega.$$

Additionally using Hölder's inequality,

$$\left| \int_{|\omega| > \epsilon^{-1}} \frac{\hat{\rho}_n(\omega)\hat{\rho}_0^*(\omega)}{|\omega|^2} d\omega \right| \leq \left( \int_{|\omega| > \epsilon^{-1}} \frac{|\hat{\rho}_n(\omega)|^2}{|\omega|^2} d\omega \right)^{\frac{1}{2}} \left( \int_{|\omega| > \epsilon^{-1}} \frac{|\hat{\rho}_0(\omega)|^2}{|\omega|^2} d\omega \right)^{\frac{1}{2}}.$$

Thus we have separated the proof of (33) into two sub-cases, one for Lipschitz functions and one for sums of point charges. We begin with the former.

**Lemma 7.** *If  $\rho \in \mathbf{L}^1(\mathbb{R}^3)$  is Lipschitz, there exists a constant  $C$  such that for any  $0 < \epsilon < 1$ ,*

$$\int_{|\omega| > \epsilon^{-1}} \frac{|\hat{\rho}(\omega)|^2}{|\omega|^2} d\omega \leq C \cdot \epsilon.$$

*Proof of lemma 7.* Since  $\rho$  is Lipschitz,

$$|\hat{\rho}(\omega)| \leq \frac{C}{1 + |\omega|}. \quad (34)$$

Therefore:

$$\begin{aligned} \int_{|\omega| > \epsilon^{-1}} \frac{|\hat{\rho}(\omega)|^2}{|\omega|^2} d\omega &\leq C \int_{|\omega| > \epsilon^{-1}} (1 + |\omega|)^{-2} \cdot |\omega|^{-2} d\omega, \\ &= C \int_0^{2\pi} \int_0^\pi \int_{\epsilon^{-1}}^\infty (1 + \alpha)^{-2} \cdot \alpha^{-2} \cdot \alpha^2 \cdot \sin \vartheta d\alpha d\vartheta d\varphi, \\ &\leq C \cdot \epsilon. \end{aligned}$$

□

For point charges we have:

**Lemma 8.** *If  $\rho$  is the sum of a finite number of point charges and  $0 < \beta < 1$ , there exists a constant  $C$  such that for any  $0 < \epsilon < 1$ ,*

$$\int_{|\omega| > \epsilon^{-1}} \frac{|\hat{\rho}(\omega)|^2}{|\omega|^2} d\omega \leq C \cdot \epsilon^\beta.$$

For the proof of lemma 8 we define a function  $\phi : \mathbb{R}^3 \rightarrow \mathbb{R}$  with prescribed decay in space and smoothness in frequency in order to approximate the point charges. The function  $\phi$  is defined through its Fourier transform. First define the following bump function:

$$b(\omega) = \begin{cases} \exp\left(-\frac{1}{1-2|\omega|^2}\right), & \text{for } |\omega| < 1/2, \\ 0, & \text{for } |\omega| \geq 1/2. \end{cases}$$

Then take:

$$\hat{\phi}(\omega) = C \cdot b * b(\omega),$$

where  $C$  is chosen so that  $\hat{\phi}(0) = 1$ . By construction,  $\hat{\phi}(0) = 1$ ,  $0 \leq \hat{\phi} \leq 1$ ,  $\text{supp } \hat{\phi} \subset \{|\omega| < 1\}$ , and  $\hat{\phi} \in C^\infty(\mathbb{R}^3)$ . In space, one has  $\phi \geq 0$ ,  $\int \phi = 1$ , and for each  $n \in \mathbb{N}$ , there exists a constant  $C_n > 0$  such that

$$\phi(u) \leq \frac{C_n}{1 + |u|^n}.$$

Define the  $s$ -dilation of  $\phi$  as:

$$\phi_s(u) = s^{-3} \phi(s^{-1}u), \quad s > 0,$$

and note that:

$$\int_{\mathbb{R}^3} \phi_s(u) du = 1, \quad 0 \leq \hat{\phi}_s \leq 1, \quad \text{and} \quad \text{supp } \hat{\phi}_s \subset \{|\omega| \leq s^{-1}\}.$$

*Proof of lemma 8.* Since  $\rho$  is the sum of point charges we write it as:

$$\rho(u) = \sum_k z_k \delta(u - r_k).$$

Let  $V(u) = |u|^{-1}$  so that  $\hat{V}(\omega) = 4\pi|\omega|^{-2}$ . Using  $\hat{\phi}_\epsilon$  and the Parseval formula we bound the quantity of interest:

$$\begin{aligned} \int_{|\omega| > \epsilon^{-1}} \frac{|\hat{\rho}(\omega)|^2}{|\omega|^2} d\omega &\leq \int_{\mathbb{R}^3} \frac{|\hat{\rho}(\omega)|^2}{|\omega|^2} (1 - \hat{\phi}_\epsilon(\omega)) d\omega, \\ &= \frac{1}{4\pi} \left( \int_{\mathbb{R}^3} |\hat{\rho}(\omega)|^2 \hat{V}(\omega) d\omega - \int_{\mathbb{R}^3} |\hat{\rho}(\omega)|^2 \hat{V}(\omega) \hat{\phi}_\epsilon(\omega) d\omega \right), \\ &= \frac{(2\pi)^3}{4\pi} \left( \sum_{k \neq l} z_k z_l \left( V(r_k - r_l) - V * \phi_\epsilon(r_k - r_l) \right) \right). \quad (35) \end{aligned}$$

Lemma 9 below proves that for each  $0 < \beta < 1$  there exists a constant  $C$  such that:

$$\forall k \neq l \text{ and } \forall \epsilon > 0, \quad |V(r_k - r_l) - V * \phi_\epsilon(r_k - r_l)| \leq C \cdot \epsilon^\beta. \quad (36)$$

Plugging (36) into (35) proves the result.  $\square$

**Lemma 9.** *For each  $0 < \beta < 1$  and  $\delta > 0$ , there exists a constant  $C$  such that for any  $\epsilon > 0$ ,*

$$\forall |u| \geq \delta, \quad |V(u) - V * \phi_\epsilon(u)| \leq C \cdot \epsilon^\beta, \quad V(u) = |u|^{-1}.$$

*Proof.* Fix  $\beta$  and  $\delta$ , and let  $n$  be an arbitrary positive integer that we will select later. Using  $\phi_\epsilon \geq 0$  and  $\int \phi_\epsilon = 1$ , we compute:

$$\begin{aligned} |V(u) - V * \phi_\epsilon(u)| &= \left| \int_{\mathbb{R}^3} \phi_\epsilon(v)(V(u) - V(u-v)) dv \right|, \\ &\leq \underbrace{\int_{|v| < \gamma} \phi_\epsilon(v)|V(u) - V(u-v)| dv}_I + \underbrace{\int_{|v| > \gamma} \phi_\epsilon(v)|V(u) - V(u-v)| dv}_II, \end{aligned}$$

where  $\gamma > 0$  is a free parameter that we will set as  $\gamma = \epsilon^\beta$  at the end of the proof.

To bound term I, we compute the modulus of continuity of  $V$  on  $|u| \geq \delta$ :

$$\forall |u|, |v| \geq \delta, \quad |V(u) - V(v)| = \frac{||v| - |u||}{|u||v|} \leq \delta^{-2}|u - v|.$$

Thus:

$$I = \int_{|v| < \gamma} \phi_\epsilon(v)|V(u) - V(u-v)| dv \leq \delta^{-2} \cdot \gamma \cdot \int_{|v| < \gamma} \phi_\epsilon(v) dv \leq \delta^{-2} \cdot \gamma.$$

Term II is more delicate and will require several steps. We begin with the following upper bound:

$$\begin{aligned} II &= \int_{|v| > \gamma} \phi_\epsilon(v)|V(u) - V(u-v)| dv, \\ &\leq \underbrace{\int_{|u-v| > \gamma} \phi_\epsilon(u-v)V(u) dv}_{II.A} + \underbrace{\int_{|u-v| > \gamma} \phi_\epsilon(u-v)V(v) dv}_{II.B}. \end{aligned}$$

The first term II.A is bounded by the following calculation:

$$\begin{aligned} II.A &= \int_{|u-v| > \gamma} \phi_\epsilon(u-v)V(u) dv \leq \delta^{-1} \int_{|v| > \gamma} \phi_\epsilon(v) dv, \\ &\leq C_n \cdot \delta^{-1} \cdot \epsilon^{n-3} \cdot \int_{|v| > \gamma} |v|^{-n} dv, \\ &\leq C(n, \delta) \cdot \epsilon^{n-3} \cdot \gamma^{3-n}, \quad \text{if } n > 3. \end{aligned}$$

Term II.B is split as:

$$\begin{aligned} \text{II.B} &= \int_{|u-v|>\gamma} \phi_\epsilon(u-v)V(v) dv, \\ &= \underbrace{\int_{\substack{|u-v|>\gamma \\ |v|<1}} \phi_\epsilon(u-v)V(v) dv}_{\text{II.B.i}} + \underbrace{\int_{\substack{|u-v|>\gamma \\ |v|>1}} \phi_\epsilon(u-v)V(v) dv}_{\text{II.B.ii}}. \end{aligned}$$

We bound II.B.i using Hölder's inequality followed by an argument similar to the one used for II.A:

$$\begin{aligned} \text{II.B.i} &= \int_{\substack{|u-v|>\gamma \\ |v|<1}} \phi_\epsilon(u-v)V(v) dv, \\ &\leq \left( \int_{|u-v|>\gamma} \phi_\epsilon(u-v)^2 dv \right)^{\frac{1}{2}} \left( \int_{|v|<1} V(v)^2 dv \right)^{\frac{1}{2}}, \\ &\leq C(n) \cdot \epsilon^{n-3} \cdot \gamma^{3/2-n}. \end{aligned}$$

Term II.B.ii is bounded with the same argument as II.A:

$$\text{II.B.ii} = \int_{\substack{|u-v|>\gamma \\ |v|>1}} \phi_\epsilon(u-v)V(v) dv \leq \int_{|v|>\gamma} \phi_\epsilon(v) dv \leq C(n) \cdot \epsilon^{n-3} \cdot \gamma^{3-n}.$$

In summary,

$$\begin{aligned} \forall |u| \geq \delta, \quad |V(u) - V * \phi_\epsilon(u)| &\leq \text{I} + \text{II.A} + \text{II.B.i} + \text{II.B.ii}, \\ &\leq C(n, \delta) \cdot (\gamma + \epsilon^{n-3} \cdot \gamma^{3-n} + \epsilon^{n-3} \cdot \gamma^{3/2-n}). \end{aligned} \quad (37)$$

Recall that  $\gamma$  and  $n$  are free parameters. Setting  $\gamma = \epsilon^\beta$  and  $n = (6-\beta)/2(1-\beta)$  completes the proof.  $\square$

## B.2 Proof of lemma 3

Recall lemma 3 from section 8.1.

**Lemma 10** (Restatement of lemma 3). *If  $\rho \in \mathbf{L}^1(\mathbb{R}^3)$  decays exponentially fast as  $|u| \rightarrow \infty$ , then:*

$$\int_\epsilon^{\epsilon^{-1}} \|\hat{\rho}_\alpha\|_2^2 d\alpha = \frac{\epsilon}{2} \left( \|\hat{\rho}_\epsilon\|_2^2 + \sum_{k=2}^{\epsilon^{-2}-1} \|\hat{\rho}_{k\epsilon}\|_2^2 + \|\hat{\rho}_{\epsilon^{-1}}\|_2^2 \right) + O(\epsilon). \quad (38)$$

*Proof.* The proof is an application of the trapezoid rule from numerical integration. Recall that it approximates the integral  $\int_a^b g(\alpha) d\alpha$  as:

$$\int_a^b g(\alpha) d\alpha = \frac{b-a}{2m} \left( g(a) + \sum_{k=2}^m 2g(\alpha_k) + g(b) \right) - \underbrace{\frac{(b-a)^3}{12m^2} g^{(2)}(\xi)}_{\text{error term}}, \quad (39)$$

where  $\alpha_k = a + (k-1)(b-a)/m$  and  $\xi \in [a, b]$ . Take  $a = \epsilon$ ,  $b = \epsilon^{-1}$ , and  $g(\alpha) = \|\hat{\rho}_\alpha\|_2^2$ . Since  $\rho$  has exponential decay,  $\hat{\rho} \in C^\infty(\mathbb{R}^3)$  with bounded derivatives of all orders. Therefore the error term can be bounded as:

$$|\text{error term}| \leq C \frac{(\epsilon^{-1} - \epsilon)^3}{m^2} = C \frac{\epsilon^3(\epsilon^{-2} - 1)^3}{m^2}.$$

Thus if  $m = \epsilon^{-2} - 1$ , the resulting error term is  $O(\epsilon)$  and (38) follows from (39).  $\square$

Since  $\hat{\rho}$  has bounded derivatives of all orders, lemma 3 can be refined to show the Coulomb energy  $U(\rho)$  can be regressed to accuracy  $O(\epsilon)$  with  $O(\epsilon^{-1-\frac{2}{n+1}})$  Fourier coefficients, for any integer  $n \geq 0$ . The parameter  $n$  corresponds to the order of the Newton-Cotes numerical integration scheme [26], where for example  $n = 0$  and  $n = 1$  correspond to the rectangle and trapezoid rules, respectively. We omit the details.

### B.3 Proof of lemma 5

Lemma 5 is proven as a corollary to lemma 2.

**Lemma 11** (Restatement of lemma 5). *Suppose that  $\psi$  satisfies:*

$$\sum_{j \in \mathbb{Z}} 2^{2j} \int_{[0, \pi]^2} |\hat{\psi}(2^j r_\theta^{-1} \omega)|^2 d\theta = |\omega|^{-2}, \quad \omega \neq 0, \quad (40)$$

and

$$\text{supp} \int_{[0, \pi]^2} |\hat{\psi}(2^j r_\theta^{-1} \omega)|^2 d\theta \subset \{c_1 2^{-j} < |\omega| < c_2 2^{-j+1}\}, \quad (41)$$

where  $0 < c_1 \leq c_2 < \infty$  are universal constants. If  $\rho$  is the sum of a Lipschitz function in  $\mathbf{L}^1(\mathbb{R}^3)$  and a finite sum of point charges, then there exists a constant  $C$  such that for any  $0 < \epsilon < 1$ ,

$$\sum_{j=-\infty}^{2 \log_2 \epsilon} 2^{2j} \|\rho * \psi_{j,\cdot}\|_2^2 \leq C \cdot \epsilon$$

and

$$\sum_{j=-\log_2 \epsilon}^{+\infty} 2^{2j} \|\rho * \psi_{j,\cdot}\|_2^2 \leq C \cdot \epsilon.$$

*Proof.* Following the proof of theorem 4,

$$\sum_{j=-\infty}^{2 \log_2 \epsilon} 2^{2j} \|\rho * \psi_{j,\cdot}\|_2^2 = \int_{\mathbb{R}^3} |\hat{\rho}(\omega)|^2 \sum_{j=-\infty}^{2 \log_2 \epsilon} 2^{2j} \int_{[0, \pi]^2} |\hat{\psi}_{j,\theta}(\omega)|^2 d\theta d\omega, \quad (42)$$

and

$$\sum_{j=\log_2 \epsilon}^{+\infty} 2^{2j} \|\rho * \psi_{j,\cdot}\|_2^2 = \int_{\mathbb{R}^3} |\hat{\rho}(\omega)|^2 \sum_{j=\log_2 \epsilon}^{+\infty} 2^{2j} \int_{[0,\pi]^2} |\hat{\psi}_{j,\theta}(\omega)|^2 d\theta d\omega. \quad (43)$$

Utilizing (41),

$$\text{supp} \sum_{j=-\infty}^{2\log_2 \epsilon} 2^{2j} \int_{[0,\pi]^2} |\hat{\psi}_{j,\theta}(\omega)|^2 d\theta \subset \{|\omega| > c_1 \epsilon^{-2}\}, \quad (44)$$

and

$$\text{supp} \sum_{j=\log_2 \epsilon}^{+\infty} 2^{2j} \int_{[0,\pi]^2} |\hat{\psi}_{j,\theta}(\omega)|^2 d\theta \subset \{|\omega| < 2c_2 \epsilon\}. \quad (45)$$

Combing (40) with (44) and (45), and plugging into (42) and (43) respectively, yields:

$$\sum_{j=-\infty}^{2\log_2 \epsilon} 2^{2j} \|\rho * \psi_{j,\cdot}\|_2^2 \leq \int_{|\omega| > c_1 \epsilon^{-2}} \frac{|\hat{\rho}(\omega)|^2}{|\omega|^2} d\omega \leq C \cdot \epsilon, \quad (46)$$

and

$$\sum_{j=\log_2 \epsilon}^{+\infty} 2^{2j} \|\rho * \psi_{j,\cdot}\|_2^2 \leq \int_{|\omega| < 2c_2 \epsilon} \frac{|\hat{\rho}(\omega)|^2}{|\omega|^2} d\omega \leq C \cdot \epsilon, \quad (47)$$

where the bound (46) follows from lemma 2, equation (33) with  $\beta = 1/2$ , and the bound (47) follows from lemma 2, equation (32).  $\square$

## References

- [1] Carlo Adamo and Vincenzo Barone. Toward reliable density functional methods without adjustable parameters: The PBE0 model. *The Journal of Chemical Physics*, 110:6158–6170, 1999. [21](#)
- [2] Joakim Andén and Stéphane Mallat. Deep scattering spectrum. *IEEE Transactions on Signal Processing*, 62(16):4114–4128, August 2014. [4](#)
- [3] T. A. Arias. Multiresolution analysis of electronic structure: semicardinal and wavelet bases. *Reviews of Modern Physics*, 71(1):267–311, January 1999. [4](#)
- [4] Albert P. Bartók and Gábor Csányi. Gaussian approximation potentials: A brief tutorial introduction. *International Journal of Quantum Chemistry*, 115:1051–1057, 2015. [3](#), [12](#), [13](#)
- [5] Albert P. Bartók, Risi Kondor, and Gábor Csányi. On representing chemical environments. *Physical Review B*, 87(18):184115(16), May 2013. [2](#), [3](#), [7](#), [12](#), [13](#), [14](#)

- [6] Albert P. Bartók, Mike C. Payne, Risi Kondor, and Gábor Csányi. Gaussian approximation potentials: The accuracy of quantum mechanics, without the electrons. *Physical Review Letters*, 104(13):136403(4), 2010. [3](#), [12](#), [13](#)
- [7] Jörg Behler. Atom-centered symmetry functions for constructing high-dimensional neural network potentials. *The Journal of Chemical Physics*, 134(7):074106, 2011. [2](#)
- [8] Jörg Behler and Michele Parrinello. Generalized neural-network representation of high-dimensional potential-energy surfaces. *Physical Review Letters*, 98(14):146401(4), 2007. [2](#), [7](#)
- [9] Thomas Blumensath and Mike E. Davies. On the difference between orthogonal matching pursuit and orthogonal least squares. Online at <http://eprints.soton.ac.uk/142469/1/BDOMPvsOLS07.pdf>, 2007. [9](#)
- [10] Joan Bruna and Stéphane Mallat. Audio texture synthesis with scattering moments. arXiv:1311.0407, 2013. [4](#)
- [11] Joan Bruna and Stéphane Mallat. Invariant scattering convolution networks. *IEEE Transactions on Pattern Analysis and Machine Intelligence*, 35(8):1872–1886, August 2013. [4](#)
- [12] Joan Bruna, Stéphane Mallat, Emmanuel Bacry, and Jean-Francois Muzy. Intermittent process analysis with scattering moments. *Annals of Statistics*, 43(1):323 – 351, 2015. [26](#)
- [13] Emmanuel Candès and Justin Romberg. Sparsity and incoherence in compressive sampling. *Inverse Problems*, 23:969–985, 2007. [8](#)
- [14] S. Chen, C. F. N. Cowan, and P. M. Grant. Orthogonal least squares learning algorithm for radial basis function networks. *IEEE Transactions on Neural Networks*, 2(2):302–309, March 1991. [8](#)
- [15] Ingrid Daubechies. *Ten Lectures on Wavelets*. Society for Industrial and Applied Mathematics, Philadelphia, PA, USA, 1992. [32](#)
- [16] Sandip De, Albert P. Bartok, Gabor Csanyi, and Michele Ceriotti. Comparing molecules and solids across structural and alchemical space. *Physical Chemistry Chemical Physics*, 18(20):13754–13769, 2016. [2](#), [3](#), [12](#), [13](#)
- [17] Peter Deglmann, Ansgar Schäfer, and Christian Lennartz. Application of quantum calculations in the chemical industry - an overview. *International Journal of Quantum Chemistry*, 115(3):107–136, 2014. [2](#)
- [18] David L. Donoho and Michael Elad. Optimally sparse representation in general (non-orthogonal) dictionaries via  $\ell_1$  minimization. *Proceedings of the National Academy of Sciences of the United States of America*, 100:2197–2202, 2003. [8](#)

- [19] David L. Donoho and Xiaoming Huo. Uncertainty principles and ideal atomic decomposition. *IEEE Transactions on Information Theory*, 47:2845–2862, 2001. [8](#)
- [20] Søren Fournais, Thomas Østergaard Sørensen, Maria Hoffmann-Ostenhof, and Thomas Hoffmann-Ostenhof. Non-isotropic cusp conditions and regularity of the electron density of molecules at the nuclei. *Annales Henri Poincaré*, 8(4):731–748, 2007. [32](#)
- [21] Luigi Genovese, Alexey Neelov, Stefan Goedecker, Thierry Deutsch, Seyed Alireza Ghasemi, Alexander Willand, Damien Caliste, Oded Zilberberg, Mark Rayson, Anders Bergman, and Reinhold Schneider. Daubechies wavelets as a basis set for density functional pseudopotential calculations. *The Journal of Chemical Physics*, 129(1):014109, 2008. [4](#)
- [22] Leslie Greengard. *The Rapid Evaluation of Potential Fields in Particle Systems*. MIT Press, Cambridge, 1988. [4](#), [33](#)
- [23] Leslie Greengard and Vladimir Rokhlin. A fast algorithm for particle simulations. *Journal of Computational Physics*, 73:325–348, 1987. [4](#), [33](#)
- [24] Johannes Hachmann, Roberto Olivares-Amaya, Sule Atahan-Evrenk, Carlos Amador-Bedolla, Roel S. Sánchez-Carrera, Aryeh Gold-Parker, Leslie Vogt, Anna M. Brockway, and Alán Aspuru-Guzik. The Harvard clean energy project: Large-scale computational screening and design of organic photovoltaics on the world community grid. *The Journal of Physical Chemistry Letters*, 2(17):2241–2251, 2011. [2](#)
- [25] Katja Hansen, Grégoire Montavon, Franziska Biegler, Siamac Fazli, Matthias Rupp, Matthias Scheffler, O. Anatole von Lilienfeld, Alexandre Tkatchenko, and Klaus-Robert Müller. Assessment and validation of machine learning methods for predicting molecular atomization energies. *Journal of Chemical Theory and Computation*, 9(8):3404–3419, 2013. [8](#), [22](#)
- [26] Joe D. Hoffman. *Numerical Methods for Engineers and Scientists*. Marcel Dekker, 2nd edition, 2001. [32](#), [41](#)
- [27] Pierre Hohenberg and Walter Kohn. Inhomogeneous electron gas. *Physical Review*, 136(3B):B864–B871, November 1964. [2](#), [5](#)
- [28] Kerwin Hui and Jeng-Da Chai. SCAN-based hybrid and double-hybrid density functionals from models without fitted parameters. *The Journal of Chemical Physics*, 144(4), 2016. 044114. [21](#), [24](#)
- [29] W. Kohn and L. J. Sham. Self-consistent equations including exchange and correlation effects. *Phys. Rev.*, 140:A1133–A1138, Nov 1965. [5](#)
- [30] Stéphane Mallat. *A Wavelet Tour of Signal Processing, Third Edition: The Sparse Way*. Academic Press, 3rd edition, 2008. [32](#)

- [31] Stéphane Mallat. Group invariant scattering. *Communications on Pure and Applied Mathematics*, 65(10):1331–1398, October 2012. [4](#), [13](#), [17](#), [18](#)
- [32] Sergei Manzhos, Xiaogang Wang, Richard Dawes, and Tucker Carrington. A nested molecule-independent neural network approach for high-quality potential fits. *The Journal of Physical Chemistry A*, 110(16):5295–5304, 2006. [2](#)
- [33] Yves Meyer. *Wavelets and Operators*, volume 1. Cambridge University Press, 1993. [32](#)
- [34] Yves Meyer and Ronald Coifman. *Wavelets: Calderón-Zygmund and Multilinear Operators*. Cambridge University Press, 2000. [32](#)
- [35] Marilyn M. Morrell, Robert G. Parr, and Mel Levy. Calculation of ionization potentials from density matrices and natural functions, and the long-range behavior of natural orbitals and electron density. *Journal of Chemical Physics*, 62(2):549–554, 1975. [32](#)
- [36] Jonathan E. Moussa. Comment on ”fast and accurate modeling of molecular atomization energies with machine learning”. *Physical Review Letters*, 109(5):059801, August 2012. [8](#)
- [37] Szilvia Nagy. *Wavelet Based Density Operators, Electron Density and Energy Functionals*. PhD thesis, Budapest University of Technology and Economics, 2005. [4](#)
- [38] Bhaarithi Natarajan, Luigi Genovese, Mark E. Casida, Thierry Deutsch, Olga N. Burchak, Christian Philouze, and Maxim Y. Balakirev. Wavelet-based linear-response time-dependent density-functional theory. *Chemical Physics*, 402:29–40, 2012. [4](#)
- [39] J. C. Pei, G. I. Fann, R. J. Harrison, W. Nazarewicz, Yue Shi, and S. Thornton. Adaptive multi-resolution 3D Hartree-Fock-Bogoliubov solver for nuclear structure. *Physical Review C*, 90(2):024317(8), 2014. [4](#)
- [40] Raghunathan Ramakrishnan, Pavlo O. Dral, Matthias Rupp, and O. Anatole von Lilienfeld. Quantum chemistry structures and properties of 134 kilo molecules. *Scientific Data*, 1:140022 EP –, 08 2014. [21](#)
- [41] Matthias Rupp, Alexandre Tkatchenko, Klaus-Robert Müller, and O. Anatole von Lilienfeld. Fast and accurate modeling of molecular atomization energies with machine learning. *Physical Review Letters*, 108(5):058301, January 2012. [2](#), [7](#), [8](#)
- [42] Ali Sadeghi, S. Alireza Ghasemi, Bastian Schaefer, Stephan Mohr, Markus A. Lill, and Stefan Goedecker. Metrics for measuring distances in configuration spaces. *The Journal of Chemical Physics*, 139(18):184118, 2013. [2](#)

- [43] Laurent Sifre and Stéphane Mallat. Rotation, scaling and deformation invariant scattering for texture discrimination. In *The IEEE Conference on Computer Vision and Pattern Recognition (CVPR)*, June 2013. [4](#), [18](#)
- [44] Viktor N. Staroverov. Density-functional approximations for exchange and correlation. In N. Sukumar, editor, *A Matter of Density: Exploring the Electron Density Concept in Chemical, Biological, and Materials Sciences*, pages 125–156. John Wiley & Sons, Hoboken, NJ, 2013. [2](#), [4](#)
- [45] Bobby G. Sumpter and Donald W. Noid. Neural networks and graph theory as computational tools for predicting polymer properties. *Macromolecular Theory and Simulations*, 3(2):363–378, 1994. [2](#)
- [46] O. Anatole von Lilienfeld, Raghunathan Ramakrishnan, Matthias Rupp, and Aaron Knoll. Fourier series of atomic radial distribution functions: A molecular fingerprint for machine learning models of quantum chemical properties. *International Journal of Quantum Chemistry*, 115:1084–1093, 2015. [2](#), [3](#), [7](#), [12](#)
- [47] Ross C. Walker, Andreas W. Götz, Luigi Genovese, Brice Videau, Damien Caliste, Jean-François Méhaut, Stefan Goedecker, and Thierry Deutsch. *Electronic Structure Calculations on Graphics Processing Units: From Quantum Chemistry to Condensed Matter Physics*, chapter 6: Wavelet-Based Density Functional Theory on Massively Parallel Hybrid Architectures. Wiley Periodicals, Inc., 2016. [4](#)
- [48] Takeshi Yanai, George I Fann, Gregory Beylkin, and Robert J Harrison. Multiresolution quantum chemistry in multiwavelet bases: excited states from time-dependent Hartree-Fock and density functional theory via linear response. *Physical Chemistry Chemical Physics*, 17(47):31405–31416, February 2015. [4](#)
- [49] Li Zhu, Maximilian Amsler, Tobias Fuhrer, Bastian Schaefer, Somayeh Faraji, Samare Rostami, S. Alireza Ghasemi, Ali Sadeghi, Migle Grauzinyte, Chris Wolverton, and Stefan Goedecker. A fingerprint based metric for measuring similarities of crystalline structures. *The Journal of Chemical Physics*, 144(3):034203, 2016. [2](#)